Shallow layer correction for Spectral Element like methods

Y. Capdeville, J.-J. Marigo

Geophys. J. Int. (2008) **172,** 1135–1150 doi: 10.1111/j.1365-246X.2007.03703.x

Shallow layer correction for Spectral Element like methods

Y. Capdeville[1] and J.-J. Marigo[2]

[1] *Équipe de sismologie, Institut de Physique du Globe de Paris, CNRS, France. E-mail: capdevil@ipgp.jussieu.fr*
[2] *Laboratoire de Modélisation en Mécanique (*UMR 7607*), Université Paris VI, France*

Accepted 2007 November 30. Received 2007 October 4; in original form 2007 July 20

SUMMARY

Today's numerical methods like the Spectral Element Method (SEM) allow accurate simulation of the whole seismic field in complex 3-D geological media. However, the accuracy of such a method requires physical discontinuities to be matched by mesh interfaces. In many realistic earth models, the design of such a mesh is difficult and quite ineffective in terms of numerical cost. In this paper, we address a limited aspect of this problem: an earth model with a thin shallow layer below the free surface in which the elastic and density properties are different from the rest of the medium and in which rapid vertical variations are allowed. We only consider here smooth lateral variations of the thickness and elastic properties of the shallow layer. In the limit of a shallow layer thickness very small compared to the smallest wavelength of the wavefield, by resorting to a second order matching asymptotic approximation, the thin layer can be replaced by a vertically smooth effective medium without discontinuities together with a specific Dirichlet to Neumann (DtN) surface boundary condition. Such a formulation allows to accurately take into account complex thin shallow structures within the SEM without the classical mesh design and time step constraints. Corrections at receivers and source—when the source is located within the thin shallow layer—have been also derived. Accuracy and efficiency of this formulation are assessed on academic tests. The stability and limitations of this formulation are also discussed.

Key words: Numerical approximations and analysis; Surface waves and free oscillations; Computational seismology; Wave propagation.

1 INTRODUCTION AND MOTIVATIONS

Over the last 10 yr, computational seismology has made important progress allowing accurate computation of the whole wavefield in complex 3-D models. In particular, the Spectral Element Method (SEM) (e.g. Priolo *et al.* 1994; Faccioli *et al.* 1996; Komatitsch & Vilotte 1998) has been shown to be very effective for large scale seismology (e.g. Komatitsch & Tromp 2002; Capdeville *et al.* 2003; Chaljub *et al.* 2003). The SEM is a high-order variational method based on hexahedra-type of mesh which, like the finite element method, can accurately take into account discontinuities of the elastic and density properties when discontinuities are matched by a mesh interface. Such a constraint leads to a lack of geometrical flexibility. Designing a cubic element mesh discretization of an earth model that honours discontinuities can be a difficult process that leads to small size elements. When using an explicit time marching scheme, such small elements impose a small time step in order to respect the stability condition, increasing dramatically the simulation cost. This is typically the case when using crustal models built on several thin layers located just below the free surface. In that case, the mesh discretization can hardly be done. So far, only crude approximations to this problem have been used. A first one is just to remove the crustal model where the mesh is too difficult to design and to replace it by a simpler model for which the mesh design is easier. A second solution is to design a mesh that does not honour the crust model discontinuity interfaces, especially the bottom Moho discontinuity interface where it gets too thin. In that case, the discontinuity interfaces do not match with a mesh interface and can be located within an element. In both solutions the accuracy cannot be warranted, and in the latter case it becomes mesh dependent and difficult to predict. To illustrate this problem, let us consider a spherically symmetric sphere, of the same radius (6371 km) as the earth, and two models.

(i) A fully homogeneous, model 1, with $V_s = 6\,\mathrm{km\,s^{-1}}$, $V_p = 8\,\mathrm{km\,s^{-1}}$ and $\rho = 3000\,\mathrm{kg\,m^{-3}}$.

(ii) A homogeneous model with a 20 km thin slow layer below the surface, model 2, with $V_s = 3\,\mathrm{km\,s^{-1}}$, $V_p = 8\,\mathrm{km\,s^{-1}}$ and $\rho = 3000\,\mathrm{kg\,m^{-3}}$, and the same properties as model 1 below 6351 km.

This simplistic example is quite representative of some of the difficulties associated with more realistic earth models like when using PReliminary Earth Model (PREM, Dziewonski & Anderson 1981), for the mantle, together with 3-D crustal models, like CRUST2.0 (Bassin *et al.* 2000) or 3SMAC (Nataf & Ricard 1996).

Simulations of a 100 s corner period wavefield are done using the coupled mode-SEM (Capdeville *et al.* 2003). The domain for the normal mode solution is defined as the domain from the centre up to 4371 km while the SEM solution domain is defined as the domain

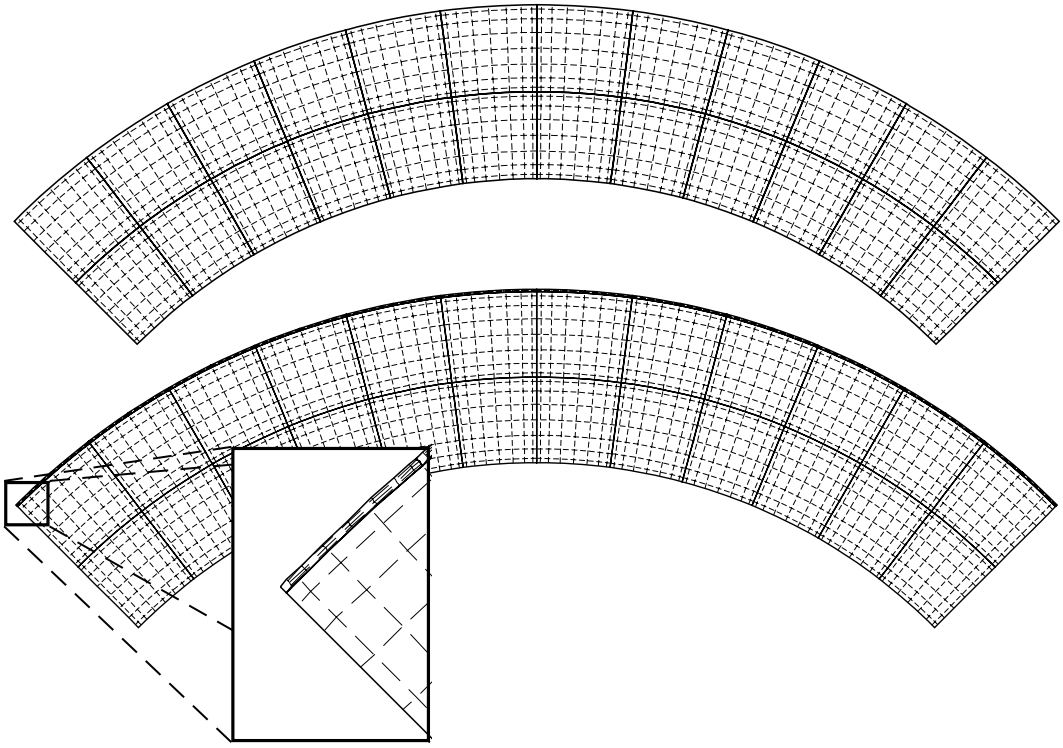

Figure 1. 2-D vertical cross-section of one region of meshes 1 (top) and 2 (bottom) used to propagate waves in, respectively, model 1 and 2 (see text). The element edges are in solid line and the integration point mesh is plotted with dashed lines. mesh 1 is made of two layers of elements and mesh 2 is made of three. The last element layer of mesh 2 is vertically so thin (20 km) compared to the 990 km edge size of the other two element layers that a zoom is needed to see it. The polynomial degree is 8 in each direction.

from 4371 km up to the surface. Three different SEM meshes have been considered.

(i) Mesh 1 (Fig. 1, top), corresponds to the discretization of model 1 with two elements of 1000 km thickness and a polynomial approximation of degree eight in each direction. For the minimum propagating wavelength considered here (roughly 600 km outside of the shallow layer), this corresponds to a two wavelength sampling for each element. Mesh 1 is slightly oversampling the wavefield.

(ii) Mesh 2 (Fig. 1, bottom), corresponds to the discretization of model 2. The 20 km thin layer below the surface is actually matched by an element layer. Vertically, mesh 2 has now three elements vertically, two of 990 km and one of 20 km size.

(iii) Mesh 2b is a relaxed version of mesh 2, where the upper elements have now a vertical thickness of 250 km instead of 20 km. For this mesh, the upper thin layer below the surface is now contained in the upper layer of elements and the discontinuity is not honoured by a mesh interface.

Stability condition for the second-order Newmark explicit time discretization leads to a time step of about 1.5 s for mesh 1 and 0.05 s for mesh 2. It is worth to note here the drastic impact of the mesh 2 discretization: computing time for mesh 2 is expected to be 30 times larger than for mesh 2. Even though this situation may be slightly improved when using a different degree for the vertical polynomial approximation in the upper layer, mesh 2 simulations will still be much more expensive than mesh 1 simulations. Computing time limitations lead in practice to fall back on simplistic approximations among which we present two. In the first one, the upper thin layer is simply ignored and model 2 is approximated using model 1 with mesh 1. A second approximation is to resort to a mesh that does not match the discontinuity interface, this is the case when using mesh 2b for the discretization of model 2. In that case, the discontinuity interface of model 2 is roughly approximated within the upper element layer. This allows to relax the time step restriction associated with mesh 2 but fail to approximate accurately the discontinuity interface. Actually, this last approximation is commonly used in practice when considering crustal models in earth global models, (e.g. Komatitsch & Tromp 2002). To assess the implications of these two choices in terms of accuracy, synthetic seismograms have been computed for two source locations, a deep one (source 1, 160 km deep) and a shallow one (source 2, 10 km deep). The source–receiver epicentral distance is 90° and the source is an arbitrary double couple moment tensor.

In Fig. 2, the synthetic seismograms corresponding to the reference solution, that is, computed for model 2 using mesh 2, and to the first crude approximation, that is, using model 1 with mesh 1, are compared. Synthetics are computed for the deep source location. For both vertical and transverse components, this type of approximation (ignoring the shallow layer) is clearly not accurate, especially for surface waves which exhibit a strong phase shift. It is quite remarkable that such a small layer can have such a large effect on seismograms. In Fig. 3, same comparison is performed but now for the second type of approximation, that is, using model 2 with mesh 2b . Even though the phase shift of the surface waves is now slightly reduced, it is still quite large. Finally, in Figs 4 and 5, the same comparisons are performed but now in the case of the shallow source location. Similar conclusions can be drawn, but these time differences in amplitude can also be clearly noted and not only for surface waves.

First this relatively extreme example shows how large the effect of a shallow structure can be, especially on surface waves phase velocity, even if the shallow structure is much thinner than the

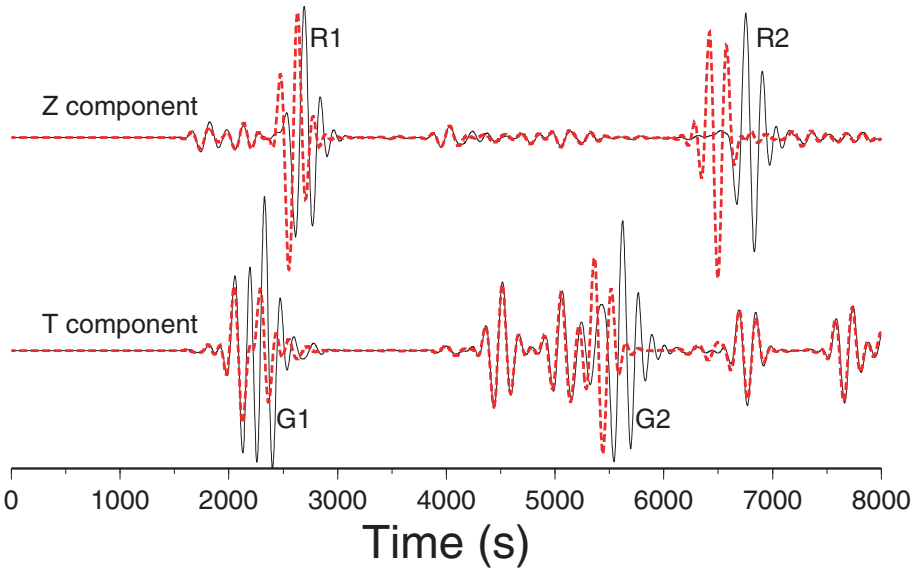

Figure 2. Comparison between reference seismograms computed in model 2 (solid line) using mesh 2 and seismograms computed in model 1 using mesh 1 (dashed line). The source is a moment tensor at 161 km depth and the epicentral distance is 92 degree. R1 and R2 phases are the minor and major arc Rayleigh surface wave trains. G1 and G2 phases are the minor and major arc Love surface wave trains. The source origin time is 500 s (this is the case for all seismograms presented in this paper).

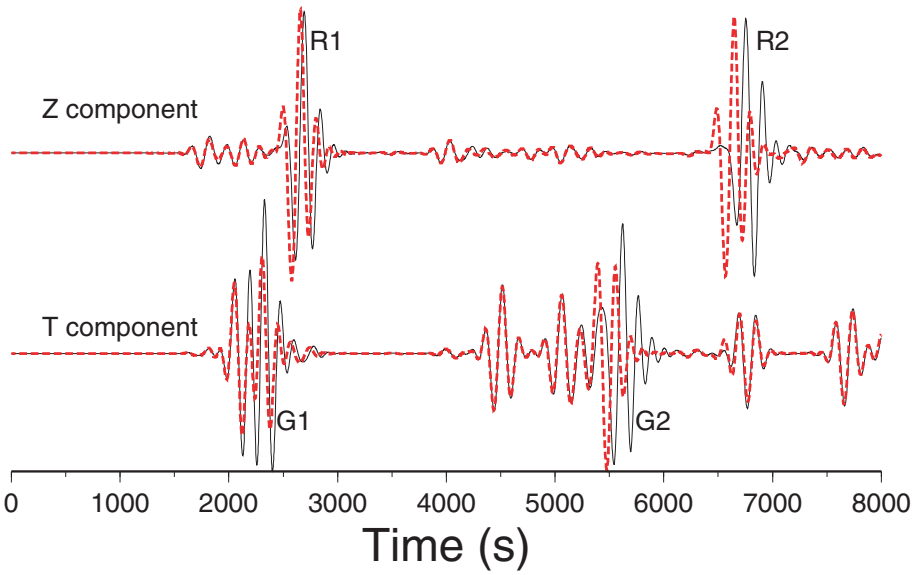

Figure 3. Same configuration and reference solution as for Fig. 2. The second solution (dashed line) is this time computed in model 2 but using mesh 2b. mesh 2b is very close to mesh 2 but with a thickness of the last spherical layer of elements of 250 km instead of 20 km for mesh 2 such that the physical discontinuity of model 2 is not matched by an element boundary.

wavelength. This fact has been known for long by seismologists working on large scale seismic imaging for whom shallow structure corrections are a constant issue (e.g. Montagner & Jobert 1988; Marone & Romanowicz 2007). Second, the results of this simple example clearly illustrate that the crude approximations classically used for simulation of complete wavefield propagation in earth models incorporating crustal models are not accurate. This problem is very close to the two scale homogenization problem used to compute effective media and effective wave equations, (see, for example Leonach & Grover 2000; Capdeville & Marigo 2007, for an application to the wave equation in layered media), but here small scales remain localized close to the free surface only. Such a boundary layer type problem has been widely study in composite material mechanics (Dumontet 1986; Abdelmoula & Marigo 2000), but very little in the wave propagation context (e.g. Boutin & Roussillon 2006). In the static context, the goal of the works simply consists in adding a first order boundary layer corrector to the leading term. To derive those correctors, a widely used technique is the matched asymptotic expansions. This formal but constructive technique is well known in the framework of fluid mechanics (to study the boundary layers of the flow near an obstacle), but was introduced more recently in solid mechanics (Nguetseng & Sanchez-Palencia 1985; Sanchez-Palencia 1987). The mathematical justification of this approach and convergence results have been obtained for some model

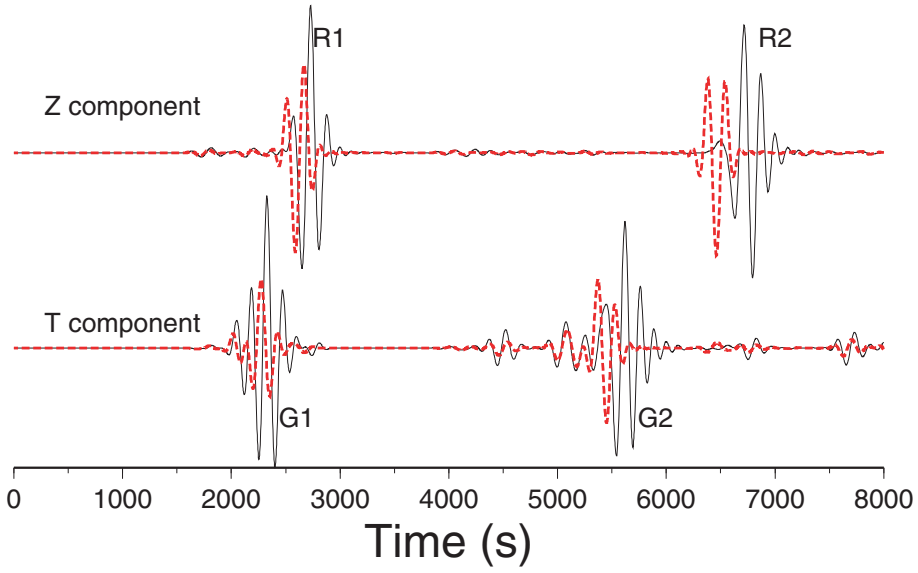

Figure 4. Same as Fig. 2 but for a 10 km depth source. The source is in the shallow layer.

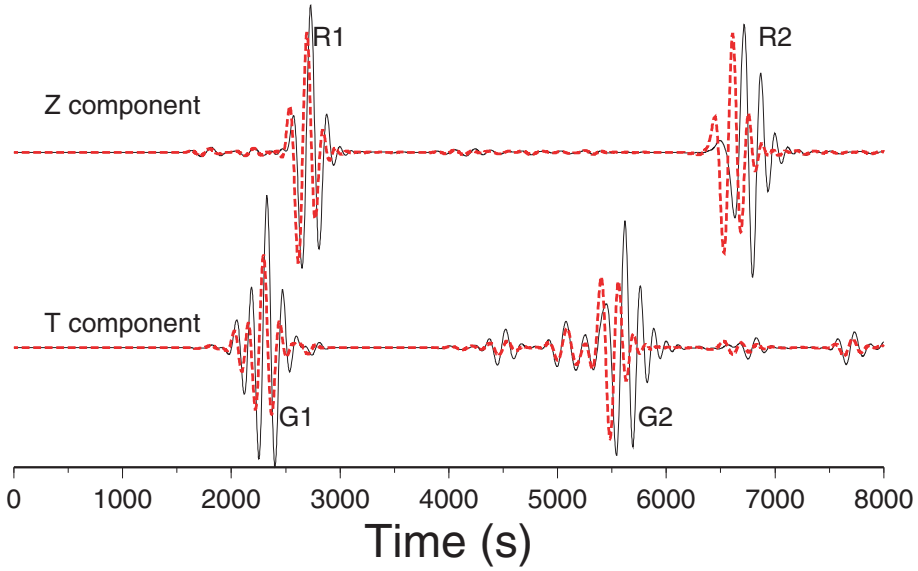

Figure 5. Same as Fig. 3 but for a 10 km depth source. The source is in the shallow layer.

problems based on Laplace-type equation with rapidly oscillating bulk coefficients or rapidly oscillating boundary conditions (Allaire & Amar 1999; Amar 2000). In this paper, we address the problem of the effective behaviour of a thin shallow layer on the wave equation. To keep the equations simple, we shall consider here the case of an infinite half-space rather than a spherically symmetric medium. However, the results obtained here can be directly extended to spherical geometry with only slight or even no modifications. We first recall the classical procedure used to solve the wave equation in such a medium using the spectral expansion in the horizontal directions. We then solve the problem by removing the shallow layer and finding the effective boundary conditions using a matching asymptotic approach. The solutions in the spectral-frequency domain are then transformed back to the space-and-time domain. The SEM implementation is provided and finally accuracy tests at the global scale are shown together with a discussion of stability and validity limitations. Even if the global scale is chosen here for the validation tests, the range of applications is not limited to this scale and can be applied, for example, at the scale of a basin with a thin sediment layer on the top.

2 THEORETICAL DEVELOPMENT

2.1 Preliminary: solving the wave equation in 1-D media

We choose here to work with an infinite half-space with material properties only varying with the vertical axis (layered medium). Working with a spherically symmetric medium would provide very similar and often exactly the same results but with some unnecessary heavier hand calculus. For the flat geometry, it is convenient to use a cylindrical coordinate system, where any position $\mathbf{x}$ can be written $\mathbf{x} = (z, r, \phi) = r\cos(\phi)\hat{\mathbf{x}} + r\sin(\phi)\hat{\mathbf{y}} + z\hat{\mathbf{z}}$ where $\hat{\mathbf{x}}$, $\hat{\mathbf{y}}$ and $\hat{\mathbf{z}}$ are the Cartesian unit vectors and z the vertical axis. We also introduce the

following notation, for any vector $\mathbf{v}$, its horizontal part is noted with an index 1: $\mathbf{v}_1 = \mathbf{v} - \mathrm{v}_z\hat{\mathbf{z}}$ with $\mathrm{v}_z = \mathbf{v}\cdot\hat{\mathbf{z}}$ the vertical part.

If gravity and anelasticity are not taken into account, the wave equation can be written

$$\rho\ddot{\mathbf{u}} - \boldsymbol{\nabla}\cdot\boldsymbol{\sigma} = \mathbf{f}, \tag{1}$$

$$\boldsymbol{\sigma} = \mathbf{c} : \boldsymbol{\epsilon}(\mathbf{u}), \tag{2}$$

where ρ is the density, $\mathbf{u}$ the displacement field, $\ddot{\mathbf{u}}$ the acceleration field, $\boldsymbol{\sigma}$ the stress tensor, $\mathbf{f}$ the source force, $\mathbf{c}$ the fourth order elastic tensor, : the double indices contraction and $\boldsymbol{\epsilon}(\mathbf{u}) = \frac{1}{2}(\boldsymbol{\nabla}\mathbf{u} + {}^T\boldsymbol{\nabla}\mathbf{u})$ the strain tensor with ^{T} the transpose operator. A free surface boundary condition is imposed at the surface ($\mathbf{t} = \boldsymbol{\sigma}\cdot\hat{\mathbf{z}} = 0$, where $\hat{\mathbf{z}}$ is the vertical axis unit vector) and the solution must vanish as z goes to minus infinity. We assume that $\mathbf{f}$ both depends upon time and space.

In layered transverse isotropic media, the 21 independent coefficients of the elastic tensor $\mathbf{c}(z)$ reduce to five, for example, the classical $A(z)$, $C(z)$, $F(z)$, $L(z)$ and $N(z)$ elastic parameters. To take advantage of the layered model assumption, we use the classical spectral expansion of the displacement and traction on a horizontal plane in the horizontal direction (e.g. Takeuchi & Saito 1972):

$$\mathbf{u}(\mathbf{x},\omega) = \int_k \sum_m [U_k(z,\omega)\mathbf{P}_{km} + V_k(z,\omega)\mathbf{B}_{km} + W_k(z,\omega)\mathbf{C}_{km}]\,\mathrm{d}k, \tag{3}$$

$$\mathbf{t}(\mathbf{x},\omega) = \boldsymbol{\sigma}(\mathbf{x},\omega)\cdot\hat{\mathbf{z}}, \tag{4}$$

$$= \int_k \sum_m [T_{Uk}(z,\omega)\mathbf{P}_{km} + T_{Vk}(z,\omega)\mathbf{B}_{km} + T_{Wk}(z,\omega)\mathbf{C}_{km}]\,\mathrm{d}k, \tag{5}$$

with

$$\mathbf{P}_{km} = Y_{km}(r,\phi)\hat{\mathbf{z}}, \tag{6}$$

$$\mathbf{B}_{km} = \frac{1}{k}\boldsymbol{\nabla}_1 Y_{km}(r,\phi), \tag{7}$$

$$\mathbf{C}_{km} = \frac{1}{k}(\hat{\mathbf{z}}\times\boldsymbol{\nabla}_1)Y_{km}(r,\phi), \tag{8}$$

where k is the horizontal wavenumber, m the azimuthal wavenumber, $\boldsymbol{\nabla}_1$ is the surface gradient vector, $Y_{km}(r,\phi) = J_m(kr)e^{im\phi}$, where J_m is the order m Bessel function of the first kind. Introducing (3) and (5) in the wave eqs (1) and (2) without the source term $\mathbf{f}$, we obtain two independent systems of equations of the form:

$$\partial_z\,{}_q\boldsymbol{\mathcal{Y}}_k(z,\omega) = {}_q\mathbf{S}_k(z,\omega)\,{}_q\boldsymbol{\mathcal{Y}}_k(z,\omega). \tag{9}$$

The index q can take two values, $q = s$ for the spheroidal (or *P-SV*) problem and $q = t$ for the toroidal (or *SH*) problem. We have ${}_s\boldsymbol{\mathcal{Y}}_k = {}^T(U_k, T_{Uk}, V_k, T_{Vk})$ for the spheroidal problem and ${}_t\boldsymbol{\mathcal{Y}}_k = {}^T(W_k, T_{Wk})$ for the toroidal problem,

$${}_s\mathbf{S}_k(z,\omega) = \begin{pmatrix} 0 & \frac{1}{C} & ka_0 & 0 \\ -\omega^2\rho & 0 & 0 & k \\ -k & 0 & 0 & \frac{1}{L} \\ 0 & -ka_0 & k^2a_1 - \omega^2\rho & 0 \end{pmatrix} \tag{10}$$

with $a_0(z) = F(z)/C(z)$, $a_1(z) = A(z) - F^2(z)/C(z)$ and

$${}_t\mathbf{S}_k(z,\omega) = \begin{pmatrix} 0 & \frac{1}{L} \\ k^2N - \omega^2\rho & 0 \end{pmatrix}. \tag{11}$$

Note that these two problems do not depend on m, which explains the fact that U_k, V_k ... have no m subscript. The free boundary conditions are $[{}_q\boldsymbol{\mathcal{Y}}(z,\omega)]_{j\in B_q} = 0$ where $[\boldsymbol{\mathcal{Y}}]_j$ is the component j of the $\boldsymbol{\mathcal{Y}}$ vector, $B_s = \{2, 4\}$ and $B_t = \{2\}$. As $z \to -\infty$, ${}_q\boldsymbol{\mathcal{Y}}_k$ must vanish.

To obtain synthetic seismograms, the classical procedure is to find a complete set of normal modes solving (9). For a given solution type q and wavenumber k, only a discrete number of frequencies ω_{qkn} are solutions. Once the eigenfunction basis is known, a synthetic seismogram is found by expanding the solution for a given source on this normal mode set:

$$\mathbf{u}(\mathbf{x},\omega) = \int_k \sum_{qnm} \frac{1}{\omega^2 - \omega_{qkn}^2}\mathbf{u}_{qkmn}(\mathbf{x})\left(\int_{\boldsymbol{\Omega}} \mathbf{u}^\star_{qkmn}.\mathbf{f}\,d\boldsymbol{\Omega}\right)\mathrm{d}k, \tag{12}$$

where $\mathbf{u}_{qknm}$ is a mode, [e.g. $\mathbf{u}_{snkm} = U_k(\omega_{kn})\,\mathbf{P}_{km} + V_k(\omega_{kn})\,\mathbf{B}_{km}$ for a spheroidal mode], $\int_{\boldsymbol{\Omega}}\mathrm{d}\boldsymbol{\Omega}$ the volume integration, * is the complex conjugate. Moreover, if $\mathbf{f}$ is a double couple point source located in $\mathbf{x}_e$ with a time history $f(t)$,

$$\mathbf{f}(\mathbf{x},\omega) = -f(\omega)\mathbf{M}\cdot\boldsymbol{\nabla}\delta(\mathbf{x} - \mathbf{x}_e) \tag{13}$$

we have

$$\int_{\boldsymbol{\Omega}} \mathbf{u}^\star_{qkmn}.\mathbf{f}\,\mathrm{d}\boldsymbol{\Omega} = f(\omega)\mathbf{M} : \boldsymbol{\epsilon}^\star_{qkmn}(\mathbf{x}_e), \tag{14}$$

$$= f(\omega)\mathbf{M} : \boldsymbol{\nabla}\mathbf{u}^\star_{qkmn}(\mathbf{x}_e), \tag{15}$$

where $\mathbf{M}$ is the (symmetric) earthquake moment tensor and $\boldsymbol{\epsilon}_{qkmn} = \boldsymbol{\epsilon}(\mathbf{u}_{qkmn})$.

For the next two sections, the wavefield will often be decomposed into two parts, one spheroidal (*P-SV*) and one toroidal (*SH*), $\mathbf{u} = \mathbf{u}^{PSV} + \mathbf{u}^{SH}$ where

$$\mathbf{u}^{PSV} = \int_k \sum_m (U_k\mathbf{P}_{km} + V_k\mathbf{B}_{km})\,\mathrm{d}k, \tag{16}$$

$$\mathbf{u}^{SH} = \int_k \sum_m W_k\mathbf{C}_{km}\,\mathrm{d}k. \tag{17}$$

Similarly, we can write $\mathbf{t} = \mathbf{t}^{PSV} + \mathbf{t}^{SH}$. The following properties can be easily demonstrated and will be useful to compute the solutions back in the space domain from the spectral domain:

$$\boldsymbol{\nabla}_1\cdot\mathbf{C}_{km} = 0, \tag{18}$$

$$\boldsymbol{\nabla}_1\times\mathbf{B}_{km} = 0, \tag{19}$$

$$\nabla_1^2\cdot\mathbf{P}_{km} = -k^2\mathbf{P}_{km}, \tag{20}$$

Using (18) and (19) we have

$$\boldsymbol{\nabla}_1\cdot\mathbf{u}^{SH} = 0, \tag{21}$$

$$\boldsymbol{\nabla}_1\times\mathbf{u}_1^{PSV} = 0. \tag{22}$$

The following classical identity will also be useful: for any regular enough vector $\mathbf{v}(\mathbf{x})$ we have

$$\nabla_1^2\mathbf{v}_1 = \boldsymbol{\nabla}_1(\boldsymbol{\nabla}_1\cdot\mathbf{v}_1) - \boldsymbol{\nabla}_1\times(\boldsymbol{\nabla}_1\times\mathbf{v}_1). \tag{23}$$

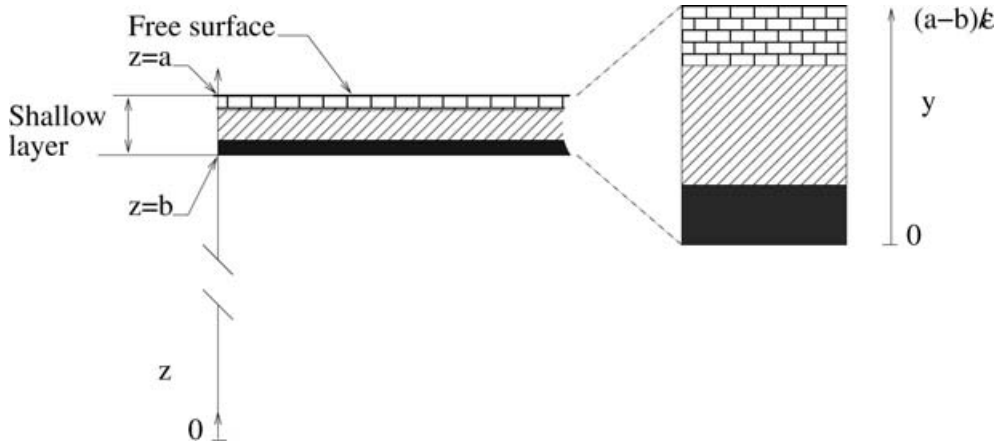

Figure 6. Sketch showing variation with z of one of the original medium property. The medium property shown here can stand for the density or elastic wave velocities.

2.2 Matching asymptotic expansions in the shallow layer

Because the following development is the same for each frequency, for each wavenumber and for the spheroidal or toroidal cases, the dependency of vectors and operators with respect to q, k and ω is dropped in this section. Because $\mathbf{S}$ operators fully define the elastic (A^s, C^s, F^s, L^s, N^s) and density (ρ^s) parameters of the model, we will often refer to $\mathbf{S}$ as an 'earth model'.

We now assume the elastic properties and density are constant or smoothly varying with depth everywhere in the model, except in a thin layer just below the surface where they are varying rapidly with z as described in Fig. 6. The top of the model is in $z = a$, the bottom of the shallow layer at $z = b_0$ and, therefore, the layer thickness is $H_0 = a - b_0$. We assume the layer to be thin with respect to the minimum wavelength of the wavefield: $\varepsilon_0 = \frac{H_0}{\lambda_{min}} \ll 1$. This defines the 'real model' $\mathbf{S}^{\varepsilon_0}$.

In the following, we assume to be given a smooth model $\mathbf{S}^s(z)$ defined on $[0, a]$ and a shallow layer model $\mathbf{S}^H(z)$ defined on $[b, a]$ of thickness $H = a - b$. $\mathbf{S}^s$ is 'smooth' in the sense that it doesn't contain any small scales and $\mathbf{S}^H$ can vary rapidly in $[b, a]$. We build $\mathbf{S}^\varepsilon$, with $\varepsilon = \frac{H}{\lambda_{min}}$, such that

$$\mathbf{S}^\varepsilon(z) = \begin{cases} \mathbf{S}^s(z) & \text{if } z < b, \\ \mathbf{S}^H(z) & \text{if } z \geq b. \end{cases} \tag{24}$$

This defines a series of models $\mathbf{S}^\varepsilon$ as ε (or b) varies. What we call the 'real model' is just a particular case of this series obtained for $\varepsilon = \varepsilon_0$ (or $b = b_0$).

In practice only the real model $\mathbf{S}^{\varepsilon_0}$ is known. $\mathbf{S}^s$ is *a priori* not given and has to be built depending on the properties of $\mathbf{S}^{\varepsilon_0}$ below b_0. For example, if the model below the depth b_0 is constant as a function of z, a valid (i.e. that doesn't depend on ε) construction is:

$$\mathbf{S}^s(z) = \begin{cases} \mathbf{S}^{\varepsilon_0}(z) & \text{if } z < b_0, \\ \mathbf{S}^{\varepsilon_0}(b_0^-) & \text{if } z \geq b_0, \end{cases} \tag{25}$$

where $\mathbf{S}^{\varepsilon_0}(b_0^-)$ is the value of $\mathbf{S}^{\varepsilon_0}$ just below b_0. For less simple cases, the $\mathbf{S}^s$ operator corresponds to a simpler model than the original model that can be any smooth prolongation of the model below the thin layer as long as it does not depend on ε. $\mathbf{S}^H$ is easily built by scaling $\mathbf{S}^{H_0}(z) = \mathbf{S}^{\varepsilon_0}(z)$ for z in $[b_0, a]$.

We introduce a new variable $y = \frac{z-b}{\varepsilon}$, a zoom on the shallow layer, such that $y = 0$ at the bottom of the layer and $y = y_a = \frac{H}{\varepsilon}$ at the free surface (see Fig. 6) as well as the $\mathbf{S}(y)$ operator:

$$\mathbf{S}(y) = \mathbf{S}^\varepsilon(\varepsilon y + b). \tag{26}$$

The main idea of this procedure is to solve the wave equation with a heavy numerical method in the smooth model $\mathbf{S}^s$ which is a much simpler task than in the original model and to use an asymptotic matching condition to compute the missing upper boundary condition. To find this missing upper boundary condition, we introduce two vectors,

(i) $\boldsymbol{\mathcal{Y}}^\varepsilon$ solution of

$$\partial_z \boldsymbol{\mathcal{Y}}^\varepsilon(z) = \mathbf{S}^s(z)\boldsymbol{\mathcal{Y}}^\varepsilon(z). \tag{27}$$

(ii) $\boldsymbol{\mathcal{D}}^\varepsilon$ solution of

$$\partial_y \boldsymbol{\mathcal{D}}^\varepsilon(y) = \varepsilon \mathbf{S}(y)\boldsymbol{\mathcal{D}}^\varepsilon(y). \tag{28}$$

The boundary conditions for (27) and (28) are a free surface boundary condition for $\boldsymbol{\mathcal{D}}^\varepsilon$ at $y = y_a$, $\boldsymbol{\mathcal{Y}}^\varepsilon$ must vanish as $z \to -\infty$ and the two solutions must match in an overlapping area which will be specified later. $\boldsymbol{\mathcal{Y}}^\varepsilon$ has a ε dependency through this last boundary condition even if its wave equation (27) doesn't depend on ε. In (28), the ε appears because of the transformation $\partial_z \to \frac{1}{\varepsilon}\partial_y$ in the original wave equation (9).

We use two asymptotic expansions for $\boldsymbol{\mathcal{Y}}^\varepsilon$ and $\boldsymbol{\mathcal{D}}^\varepsilon$:

$$\boldsymbol{\mathcal{Y}}^\varepsilon(z) = \sum_{i=-1}^{\infty} \varepsilon^i \boldsymbol{\mathcal{Y}}^i(z), \tag{29}$$

$$\boldsymbol{\mathcal{D}}^\varepsilon(y) = \sum_{i=-1}^{\infty} \varepsilon^i \boldsymbol{\mathcal{D}}^i(y). \tag{30}$$

The sums start at $i = -1$ because we will see later that the first terms non-trivialy equal to zero starts at $i = -1$. Introducing these expansions into (27) and (28), for each i, we obtain

$$\partial_z \boldsymbol{\mathcal{Y}}^i = \mathbf{S}^s \boldsymbol{\mathcal{Y}}^i \tag{31}$$

$$\partial_y \boldsymbol{\mathcal{D}}^{i+1} = \mathbf{S}\boldsymbol{\mathcal{D}}^i. \tag{32}$$

The boundary conditions are

$$[\boldsymbol{\mathcal{D}}^i]_{j \in B} = 0 \text{ for } y = y_a, \tag{33}$$

$$\boldsymbol{\mathcal{Y}}^i \to 0 \text{ as } z \to -\infty. \tag{34}$$

$\boldsymbol{\mathcal{D}}^i$ and $\boldsymbol{\mathcal{Y}}^i$ must match somewhere. (35)

For the third boundary condition, we assume there exists a large negative y where the solution $\boldsymbol{\mathcal{D}}^\varepsilon(y)$ is still valid as well as $\boldsymbol{\mathcal{Y}}^\varepsilon(\varepsilon y+b)$ such $\boldsymbol{\mathcal{D}}^\varepsilon(y) = \boldsymbol{\mathcal{Y}}^\varepsilon(\varepsilon y + b)$. In the limit when ε tends towards zero, even if $-y$ is large, $\varepsilon\, y + b$ is close to a and, therefore, a Taylor expansion for $\boldsymbol{\mathcal{Y}}^i$ around a can be used:

$$\boldsymbol{\mathcal{Y}}^I[a+\varepsilon(y-y_a)] = \sum_{j=0}^{\infty} \varepsilon^j \frac{(y-y_a)^j}{j!} \frac{\partial^j \boldsymbol{\mathcal{Y}}^i}{\partial z^j}(a). \tag{36}$$

Introducing (36) in (29) and imposing that the two solutions $\boldsymbol{\mathcal{D}}^\varepsilon$ and $\boldsymbol{\mathcal{Y}}^\varepsilon$ match for very large $-y$, we find the matching conditions:

$$\lim_{y\to-\infty} \boldsymbol{\mathcal{D}}^i(y) - \sum_{j=0}^{i} \frac{(y-y_a)^{i-j}}{(i-j)!} \frac{\partial^{i-j}\boldsymbol{\mathcal{Y}}^j}{\partial z^{i-j}}(a) = 0. \tag{37}$$

Eqs (31) and (32) have now to be solved for each i with the boundary conditions (33) and (34) and the matching conditions (37).

For $i < -2$, we obtain $\boldsymbol{\mathcal{D}}^{i+1} = \boldsymbol{\mathcal{Y}}^{i+1} = 0$.

For $i = -2$, (32) gives $\partial_y \boldsymbol{\mathcal{D}}^{-1} = 0$. With the boundary conditions and matching condition, the only solution to the previous equation is $\boldsymbol{\mathcal{D}}^{-1} = 0$, which also impose $\boldsymbol{\mathcal{Y}}^{-1} = 0$.

For $i = -1$, (32) gives $\partial_y \boldsymbol{\mathcal{D}}^0 = 0$. $\boldsymbol{\mathcal{D}}^0$ is, therefore, constant in the shallow layer. The matching condition gives $\boldsymbol{\mathcal{D}}^0 = \boldsymbol{\mathcal{Y}}^0(a)$. These expected results show that the shallow layer has no effect on the solution $\boldsymbol{\mathcal{Y}}$ at order 0. Neglecting the shallow layer by just ignoring it and replacing it by the smooth model is, therefore, an order zero approximation.

For $i = 0$, (32) gives

$$\partial_y \boldsymbol{\mathcal{D}}^1 = \mathbf{S}\boldsymbol{\mathcal{D}}^0. \tag{38}$$

Knowing that $\boldsymbol{\mathcal{D}}^0$ is constant in y and $\boldsymbol{\mathcal{D}}^0 = \boldsymbol{\mathcal{Y}}^0(a)$, the last equation can easily be integrated:

$$\boldsymbol{\mathcal{D}}^1(y) = \boldsymbol{\mathcal{D}}^1(y_a) + \left[\int_{y_a}^{y} \mathbf{S}(y')\,\mathrm{d}y'\right] \boldsymbol{\mathcal{Y}}^0(a). \tag{39}$$

The matching condition for $i = 1$ gives

$$\lim_{y\to-\infty} \left[\boldsymbol{\mathcal{D}}^1(y) - (y-y_a)\partial_z \boldsymbol{\mathcal{Y}}^0(a) - \boldsymbol{\mathcal{Y}}^1(a)\right] = 0. \tag{40}$$

Knowing that $\mathbf{S}\,(y) = \mathbf{S}^s(\varepsilon y + b)$ for $y < 0$, using (31) for $i = 0$ and (39), the matching condition (40) gives

$$\boldsymbol{\mathcal{D}}^1(y_a) - \boldsymbol{\mathcal{Y}}^1(a) + \mathbf{X}^1(0)\boldsymbol{\mathcal{Y}}^0(a) = 0, \tag{41}$$

with

$$\mathbf{X}^1(y) = -\int_{y}^{y_a} \left[\mathbf{S}(y') - \mathbf{S}^s(a)\right]\,\mathrm{d}y'. \tag{42}$$

Eq. (41) makes the link between the two solutions $\boldsymbol{\mathcal{D}}^1$ and $\boldsymbol{\mathcal{Y}}^1$. Using $[\boldsymbol{\mathcal{D}}^1(y_a)]_{i\in B} = 0$, it gives the boundary conditions for $\boldsymbol{\mathcal{Y}}^1$ in $z = a$:

$$\left[\boldsymbol{\mathcal{Y}}^1(a)\right]_{i\in B} = \left[\mathbf{X}^1(0)\boldsymbol{\mathcal{Y}}^0(a)\right]_{i\in B}. \tag{43}$$

For $i = 1$, (32) gives

$$\partial_y \boldsymbol{\mathcal{D}}^2 = \mathbf{S}\boldsymbol{\mathcal{D}}^1. \tag{44}$$

Integrating the last equation, we find

$$\begin{aligned}\boldsymbol{\mathcal{D}}^2(y) = \boldsymbol{\mathcal{D}}^2(y_a) &+ \left\{\int_{y_a}^{y} \mathbf{S}(y')[\mathbf{X}^1(y') - \mathbf{X}^1(0)]\,\mathrm{d}y'\right\} \boldsymbol{\mathcal{Y}}^0(a)\\ &+ \left[\int_{y_a}^{y} (y'-y_a)\mathbf{S}(y')\,\mathrm{d}y'\right] \mathbf{S}^s(a)\boldsymbol{\mathcal{Y}}^0(a)\\ &+ \left[\int_{y_a}^{y} \mathbf{S}(y')\,\mathrm{d}y'\right] \boldsymbol{\mathcal{Y}}^1(a).\end{aligned} \tag{45}$$

The matching condition for $i = 2$ is

$$\lim_{y\to-\infty} \left[\boldsymbol{\mathcal{D}}^2(y) - \frac{1}{2}(y-y_a)^2\partial_{z^2}^2 \boldsymbol{\mathcal{Y}}^0(a) - (y-y_a)\partial_z \boldsymbol{\mathcal{Y}}^1(a) - \boldsymbol{\mathcal{Y}}^2(a)\right] = 0. \tag{46}$$

Knowing that $\mathbf{S}(y) = \mathbf{S}^s(\varepsilon y + b)$ for $y < 0$, using (31) for $i = 0$ and (45), the matching condition (46) gives

$$\boldsymbol{\mathcal{D}}^2(y_a) + \mathbf{X}^2(0)\boldsymbol{\mathcal{Y}}^0(a) + \mathbf{X}^1(0)\boldsymbol{\mathcal{Y}}^1(a) - \boldsymbol{\mathcal{Y}}^2(a) = 0, \tag{47}$$

with

$$\mathbf{X}^2(y) = -\int_{y}^{y_a} \{\mathbf{S}(y')[\mathbf{X}^1(y') - \mathbf{X}^1(0)] - [\mathbf{X}^1(y') - \mathbf{X}^1(0)]\mathbf{S}^s(a)\}\,\mathrm{d}y'. \tag{48}$$

To obtain the last equation, we have assumed that $\partial_z \mathbf{S}^s(a) \ll \mathbf{S}^s(a)$ which implies we have been able to build a smooth model that does not vary much in the thin shallow layer with respect to its absolute value. This assumption is easy to meet for the earth. Nevertheless, when this assumption is not valid, one can with some algebra but no real difficulty complete the last expression. Finally, using $[\boldsymbol{\mathcal{D}}^2(y_a)]_{i\in B} = 0$, (47) gives the boundary conditions for $\boldsymbol{\mathcal{Y}}^2$ in $z = a$:

$$\left[\boldsymbol{\mathcal{Y}}^2(a)\right]_{i\in B} = \left[\mathbf{X}^2(0)\boldsymbol{\mathcal{Y}}^0(a) + \mathbf{X}^1(0)\boldsymbol{\mathcal{Y}}^1(a)\right]_{i\in B}. \tag{49}$$

We are now able to solve eqs (31) and (32) for order 0, 1 and 2. Nevertheless, it is not very convenient for methods like SEM to solve different orders one after another. Instead of doing so, it is more interesting to somehow solve for the sum of all orders. To do so, we solve for $\hat{\boldsymbol{\mathcal{Y}}}^2$ and $\hat{\boldsymbol{\mathcal{D}}}^2$, solutions of (27) and (28), respectively, with the free boundary condition at the surface and regularity of the solution as $z \to -\infty$ but with the following matching condition:

$$\hat{\boldsymbol{\mathcal{D}}}^2\left(\frac{a-b}{\varepsilon}\right) = \left[\mathbf{I} - \varepsilon\hat{\mathbf{X}}^2(0)\right]\hat{\boldsymbol{\mathcal{Y}}}^2(a), \tag{50}$$

with

$$\hat{\mathbf{X}}^2(y) = \mathbf{X}^1(y) + \varepsilon\mathbf{X}^2(y). \tag{51}$$

One can check that

$$\hat{\boldsymbol{\mathcal{Y}}}^2 = \boldsymbol{\mathcal{Y}}^0 + \varepsilon\boldsymbol{\mathcal{Y}}^1 + \varepsilon^2\boldsymbol{\mathcal{Y}}^2 + O(\varepsilon^3), \tag{52}$$

$$\hat{\boldsymbol{\mathcal{D}}}^2 = \boldsymbol{\mathcal{D}}^0 + \varepsilon\boldsymbol{\mathcal{D}}^1 + \varepsilon^2\boldsymbol{\mathcal{D}}^2 + O(\varepsilon^3). \tag{53}$$

The source and the receiver are often located in the shallow layer and it is useful to know $\hat{\boldsymbol{\mathcal{D}}}^2[(z-b)/\varepsilon]$ as a function of $\hat{\boldsymbol{\mathcal{Y}}}^2(z)$. It can be shown that, for $z > b$,

$$\hat{\boldsymbol{\mathcal{D}}}^2\left(\frac{z-b}{\varepsilon}\right) = \left\{\mathbf{I} - \varepsilon\left[\hat{\mathbf{X}}^2(0) - \hat{\mathbf{X}}^2\left(\frac{z-b}{\varepsilon}\right)\right]\right\}\hat{\boldsymbol{\mathcal{Y}}}^2(z), \tag{54}$$

For double-couple sources, it is useful to know the first derivative of the solution with respect to z in the shallow layer:

$$\begin{aligned}&\partial_z\hat{\boldsymbol{\mathcal{D}}}^2\left(\frac{z-b}{\varepsilon}\right)\\ &= \mathbf{S}^\varepsilon(z)\left\{\mathbf{I} - \varepsilon\left[\hat{\mathbf{X}}^2(0) - \hat{\mathbf{X}}^2\left(\frac{z-b}{\varepsilon}\right)\right]\right\}\hat{\boldsymbol{\mathcal{Y}}}^2(z) + O(\varepsilon^3).\end{aligned} \tag{55}$$

The expressions obtained here are very similar to the ones obtained by Capdeville & Marigo (2007) which indicates that the transition from this shallow layer correction to the more general homogenization case should be straightforward.

2.3 From the horizontal spectral domain to the space domain

In order to use the results obtained in the previous section with numerical methods based on a space formulation, one needs to convert them from the horizontal spectral domain to the space domain. This has to be done for the boundary condition in any case and for the source and the receiver when they are located in the shallow layer. In the following, we name $\mathbf{u}$ and $\mathbf{t}$ the displacement and traction corresponding to the $\hat{\boldsymbol{\mathcal{Y}}}$ solution and $\mathbf{u}^c$ and $\mathbf{t}^c$ the displacement and traction corresponding to the $\hat{\boldsymbol{\mathcal{D}}}$ solution corrected for the shallow layer effect. More generally, all quantities (vector components, strain tensor ...) corresponding to the $\hat{\boldsymbol{\mathcal{D}}}$ solution are noted with a '^{c}' upper script.

2.3.1 Boundary conditions

We explicit here the spectral to space domain conversion only for the first order of the toroidal case. The complete case is given in Appendix A. The matching condition (50) gives

$$\left[(\mathbf{I} - \varepsilon\, {}_t\hat{\mathbf{X}}^1_k)_t \hat{\boldsymbol{\mathcal{Y}}}^1_k\right]_2 (a) = 0, \tag{56}$$

which, using (11) and (42) can be written

$$T_{Wk}(a,\omega) = \varepsilon\left[k^2 X^1_N(0) - \omega^2 X^1_\rho(0)\right] W_k(a,\omega), \tag{57}$$

where

$$X^1_N(y) = -\int_y^{y_a} [N(y') - N^s(a)]\,\mathrm{d}y' \tag{58}$$

$$X^1_\rho(y) = -\int_y^{y_a} [\rho(y') - \rho^s(a)]\,\mathrm{d}y' \tag{59}$$

with $N(y) = N^\varepsilon(\varepsilon y + b)$, $\rho(y) = \rho^\varepsilon(\varepsilon y + b)$. Using (3), (5), (20) and returning to the time domain, for all $\mathbf{x}$ belonging to the free surface, to the first order we have:

$$\mathbf{t}^{SH}(\mathbf{x},t) = -\varepsilon\left[X^1_N(0)\,\nabla^2_1 \mathbf{u}^{SH}(\mathbf{x},t) - X^1_\rho(0)\,\ddot{\mathbf{u}}^{SH}(\mathbf{x},t)\right]. \tag{60}$$

In practice, the toroidal part and spheroidal part of a wavefield cannot be accessed and only the total wavefield $\mathbf{u}$ is known. If $\mathbf{u}$ is used instead of $\mathbf{u}^{SH}$ in (60), because $\nabla^2_1\mathbf{u} = \nabla^2_1\mathbf{u}^{SH} + \nabla^2_1\mathbf{u}^{PSV}$ and $\nabla^2_1\mathbf{u}^{PSV}$ is in general non-zero, there will be an unwanted contribution of the spheroidal part of the displacement on the toroidal traction. To avoid this problem, the identity (23) and the property (21) can be used to show that

$$\nabla^2_1\mathbf{u}^{SH} = -\boldsymbol{\nabla}_1 \times \boldsymbol{\nabla}_1 \times \mathbf{u}_1 \tag{61}$$

and, therefore, for all $\mathbf{x}$ belonging to the free surface, we have

$$\mathbf{t}^{SH}(\mathbf{x},t) = \varepsilon\left[X^1_N(0)\,\boldsymbol{\nabla}_1 \times \boldsymbol{\nabla}_1 \times \mathbf{u}_1(\mathbf{x},t) + X^1_\rho(0)\,\ddot{\mathbf{u}}^{SH}(\mathbf{x},t)\right]. \tag{62}$$

Note that the problem may seem to be not completely cleared because of the last term of the last equation still depends on $\mathbf{u}^{SH}$. Nevertheless, it is shown in Appendix A that the exact same term appears in the spheroidal part of the solutions and, therefore, it is safe to replace $\mathbf{u}^{SH}$ by $\mathbf{u}$ here.

As mentioned earlier, the complete expression of the traction on the free boundary is given in Appendix A, and has the form, for all $\mathbf{x}$ belonging to the free surface and all times t,

$$\mathbf{t} = \boldsymbol{\mathcal{A}}^\varepsilon(\mathbf{u}, \ddot{\mathbf{u}}). \tag{63}$$

Because the last equation is a boundary condition in traction that depends upon the displacement, it is called a Dirichlet to Neumann condition (DtN).

2.3.2 Receiver correction

Most of the time, the receivers are located on the free surface and, therefore, a shallow layer correction must be applied. This time, the solution needed is $\hat{\boldsymbol{\mathcal{D}}}(y_a)$ knowing $\hat{\boldsymbol{\mathcal{Y}}}(a)$ given by (50). Up to the order 1, using (50) for the first component in the toroidal case, and the first and third component in the spheroidal case, we find, for a receiver located in $\mathbf{x}_r$,

$$\mathbf{u}^c(\mathbf{x}_r,t) = \mathbf{u}(\mathbf{x}_r,t) + \varepsilon X^1_{a0}(0)\,(\boldsymbol{\nabla}_1 \cdot \mathbf{u}_1)(\mathbf{x}_r,t)\,\hat{\mathbf{z}}, \tag{64}$$

where X^1_{a0} is given in Appendix A. It can be seen that, to order 1 in ε, only the vertical component of the spheroidal case has a non-zero correction. The order 2 correction for the receiver has not been used in this paper.

2.3.3 Sources located in the shallow layer

If the source is located in the shallow layer, a correction also needs to be applied. As shown in eq. (15), the moment tensors is applied to the strain tensor. Using (54) and (55) in $y = (z_e - b)/\varepsilon$, where z_e is the vertical location of the source, we can find $\mathbf{M}^c : \boldsymbol{\nabla}\mathbf{u}^c(\mathbf{x}_e)$ as a function of $\mathbf{u}$. $\mathbf{M}^c$ is the 'real' moment tensor used to compute the solution in the original model underlying $\mathbf{S}^\varepsilon$. As for the receiver correction, we limit the asymptotic expansion to the order 1. Only the toroidal case is developed here, the spheroidal case is given in Appendix B. We have, for any symmetric $\mathbf{M}$:

$$\mathbf{M} : \boldsymbol{\nabla}\mathbf{u} = \mathbf{M}_{11} : \boldsymbol{\epsilon}_{11} + \mathbf{M}_{1z} \cdot (\boldsymbol{\nabla}_1 \mathrm{u}_z + \partial_z \mathbf{u}_1) + M_{zz}\mathrm{u}_z, \tag{65}$$

where $\boldsymbol{\epsilon}_{11} = \frac{1}{2}(\boldsymbol{\nabla}_1\mathbf{u}_1 + {}^T\boldsymbol{\nabla}_1\mathbf{u}_1)$,

$$\mathbf{M}_{1z} = {}^T(M_{rz}, M_{\phi z}, 0), \tag{66}$$

$$\mathbf{M}_{11} = \begin{pmatrix} M_{rr} & M_{r\phi} & 0 \\ M_{\phi r} & M_{\phi\phi} & 0 \\ 0 & 0 & 0 \end{pmatrix}. \tag{67}$$

Considering the following toroidal displacement for any k and m,

$$\mathbf{u}^c = W^c_k \mathbf{C}_{km}, \tag{68}$$

we have

$$\mathbf{M}^c : \boldsymbol{\nabla}\mathbf{u}^c = \mathbf{M}^c_{11} : \boldsymbol{\epsilon}^c_{11} + \mathbf{M}^c_{1z} \cdot \partial_z \mathbf{u}^c_1, \tag{69}$$

$$= W^c_k\,\mathbf{M}^c_{11} : \boldsymbol{\nabla}\mathbf{C}_{km} + \frac{1}{L^\varepsilon_e} T^c_{Wk} \mathbf{M}^c_{1z} \cdot \mathbf{C}_{km}, \tag{70}$$

where $L^\varepsilon_e = L^\varepsilon(z_e)$ and the relation $\partial_z W^c_k = \frac{1}{L^\varepsilon_e} T^c_{Wk}$ has been used. Using (54) in the toroidal case, we find, to the first order

$$W^c_k = W_k - \varepsilon L_e X^1_{eL} \partial_z W_k, \tag{71}$$

$$T^c_{Wk} = L_e \partial_z W_k - \varepsilon\left(k^2 X^1_{eN} - \omega^2 X^1_{e\rho}\right) W_k, \tag{72}$$

where

$$X^1_L(y) = -\int_y^{y_a} \left[\frac{1}{L}(y') - \frac{1}{L^s}(a)\right] \mathrm{d}y', \tag{73}$$

$$X^1_{eL} = X^1_L(0) - X^1_L\left(\frac{z_e - b}{\varepsilon}\right), \tag{74}$$

$$X^1_{eN} = X^1_N(0) - X^1_N\left(\frac{z_e - b}{\varepsilon}\right), \tag{75}$$

$$X^1_{e\rho} = X^1_\rho(0) - X^1_\rho\left(\frac{z_e - b}{\varepsilon}\right), \tag{76}$$

with $L(y) = L^\varepsilon(\varepsilon y + b)$. Using (3), (20), (23), the property (21) and the symmetry of the moment tensor, we can show that

$$\begin{aligned}\mathbf{M}^c : \boldsymbol{\epsilon}^{c\,SH} = {} & \mathbf{M}^0_{1z} \cdot \boldsymbol{\epsilon}^{SH}_{1z} - \varepsilon \frac{X^1_{eN}}{L^s}\mathbf{M}^0_{1z} \cdot (\boldsymbol{\nabla}_1 \times \boldsymbol{\nabla}_1 \times \mathbf{u}_1) \\ & + \varepsilon\omega^2 \frac{X^1_{e\rho}}{L^s}\mathbf{M}^0_{1z} \cdot \mathbf{u}^{SH} - \varepsilon X^1_{eL} L^s \mathbf{M}^c_{11} : \partial_z \boldsymbol{\epsilon}^{SH}_{11},\end{aligned} \tag{77}$$

where $\mathbf{M}^0_{1z} = \frac{L^s_e}{L^\varepsilon_e}\mathbf{M}^c_{1z}$ and $L^s_e = L^s(z_e)$. It appears clearly here that, for a moment tensor source, there is an order 0 effect of the shallow layer through the L^s_e/L^ε_e ratio. The $\mathbf{M}^0$ moment tensor (see Appendix B for complete expression) is the order 0 apparent moment tensor. If located outside of the shallow layer, we have $\mathbf{M}^0 = \mathbf{M}^c$ but not if source is located in the shallow layer. Including the time dependence $f(t)$ of the source (77) can be rewritten as a force vector,

$$\mathbf{f}(\mathbf{x}, t) = \mathcal{F}[f(t)\delta(\mathbf{x} - \mathbf{x}_e)], \tag{78}$$

where for any scalar function $g(\mathbf{x}, t)$

$$\begin{aligned}\mathcal{F}(g) = {} & \mathbf{M}^0_{1z} \cdot \boldsymbol{\nabla}_1 g\, \hat{\mathbf{z}} - \varepsilon \frac{X^1_{eN}}{L^s_e}\boldsymbol{\nabla}_1 \times \boldsymbol{\nabla}_1 \times \mathbf{M}^0_{1z} g \\ & - \varepsilon \frac{X^1_{e\rho}}{L^s_e}\mathbf{M}^0_{1z}\ddot{g} - \varepsilon X^1_{eL} L^s_e \mathbf{M}^c_{11}\boldsymbol{\nabla}_1 g.\end{aligned} \tag{79}$$

To be complete, the spheroidal part of the solution needs to be included in the source correction. This is done in Appendix B.

2.4 Spectral element implementation

We now consider a bounded domain $\boldsymbol{\Omega}$ that can be a part of the infinite half-space or the whole Earth (in the spherical geometry case) and its boundary $\partial\boldsymbol{\Omega}$. In the infinite half-space, we consider that $\partial\boldsymbol{\Omega}$ is limited to the free surface and that a solution is found for the other faces of the domain (like absorbing boundaries). The SEM solves the wave equation under the weak form, that is, the solution $\mathbf{u}$, for all admissible displacements $\mathbf{w}$ and all times t must satisfy

$$(\rho\ddot{\mathbf{u}}, \mathbf{w}) + a(\mathbf{u}, \mathbf{w}) - \langle \mathbf{t}, \mathbf{w}\rangle_{\partial\boldsymbol{\Omega}} = (\mathbf{f}, \mathbf{w}) \tag{80}$$

with $(\mathbf{w}, \rho\mathbf{u})|_{t=0} = 0$ and $(\mathbf{w}, \rho\dot{\mathbf{u}})|_{t=0} = 0$, where $(\cdot, \cdot)$ is the classical L^2 inner product, the symmetric elastic bi-linear form

$$a(\mathbf{u}, \mathbf{w}) = \int_{\boldsymbol{\Omega}} \boldsymbol{\nabla}\mathbf{u} : \mathbf{c} : \boldsymbol{\nabla}\mathbf{w}\, \mathrm{d}\mathbf{x} \tag{81}$$

and

$$\langle \mathbf{t}, \mathbf{w}\rangle_{\partial\boldsymbol{\Omega}} = \int_{\partial\boldsymbol{\Omega}} \mathbf{t} \cdot \mathbf{w}\, \mathrm{d}\mathbf{x}. \tag{82}$$

Usually the term $\langle \mathbf{t}, \mathbf{w}\rangle_{\partial\Omega}$ vanishes because of the free boundary condition. In our case, we have

$$\langle \mathbf{t}, \mathbf{w}\rangle_{\partial\boldsymbol{\Omega}} = \int_{\partial\boldsymbol{\Omega}} \boldsymbol{\mathcal{A}}^\varepsilon(\mathbf{u}, \ddot{\mathbf{u}}) \cdot \mathbf{w}\ \ \mathrm{d}\mathbf{x}, \tag{83}$$

where $\boldsymbol{\mathcal{A}}^\varepsilon$ is defined in eq. (A16).

If the source happens to be located in the shallow layer, the source term $(\mathbf{f}, \mathbf{w})$ can be computed from eq. (B11).

The classical spectral element approximation can then be applied without any major difficulty, at least for the first order. The boundary condition term requires to compute terms with gradient and curl on a surface, like for example, for the toroidal contribution:

$$\langle \boldsymbol{\nabla}_1 \times \boldsymbol{\nabla}_1 \times \mathbf{u}_1, \mathbf{w}\rangle_{\partial\boldsymbol{\Omega}} = \int_{\partial\boldsymbol{\Omega}} (\boldsymbol{\nabla}_1 \times \mathbf{w}_1) \cdot (\boldsymbol{\nabla}_1 \times \mathbf{u}_1)\, \mathrm{d}\mathbf{x}, \tag{84}$$

where the Green's theorem has been used. In flat geometry, computing terms like (84) is straightforward, but in spherical geometry this is less simple. Indeed, because of the pole singularities, the spherical coordinates cannot be used. Instead, the local coordinates of the 'cubed sphere' are used (Sadourny 1972; Ronchi *et al.* 1996). These local coordinates system are non-orthogonal curvilinear systems leading to less simple expressions than in the flat case. Nevertheless, with some patience, these expressions can be retrieved and computed without any numerical difficulty. The second order terms are potentially problematic. Indeed, as presented in Appendix A, the DtN operator $\boldsymbol{\mathcal{A}}^\varepsilon$ leads to terms in (81) which involve third order spatial derivatives, which is not compatible with C^0 spectral elements. Even if most of the terms of $\langle \mathbf{t}, \mathbf{w}\rangle_{\partial\Omega}$ can be symmetrize (see Appendix A) and the problem of the third order spatial derivatives can be worked out by introducing auxiliary variables (Givoli 2004; Givoli *et al.* 2006) or by using a spatial filtering to remove unphysical small spatial frequencies of $\mathbf{u}$ before using it in $\boldsymbol{\mathcal{A}}^\varepsilon$, none of these solution is used here. Instead, we commit a variational crime (Strang & Fix 1973) by implementing the second order DtN term as it is given in Appendix A, which appears to give an accurate solution, at least for cases shown in this paper. Nevertheless, proper solutions to this problem will be explored in future works.

For the time evolution, a classical explicit Newmark time marching scheme is used. With the introduction of the DtN boundary condition (83), because of its dependency on acceleration, this time marching scheme becomes implicit. This problem is similar to the one obtained when coupling a normal solution with the SEM through a DtN operator (see Capdeville *et al.* 2003). The order 1 acceleration terms can be included in the mass matrix, but the order 2 terms have to be treated implicitly. Nevertheless, this modification is minor and localized on the surface of the mesh. From the stability point of view, the DtN boundary condition can be a problem depending on the elastic, the density contrast and on the thickness of the shallow layer. For example, the order 1 acceleration terms, once included in the mass matrix, can lead to a locally negative mass matrix for mesh points localized on the surface. Obviously, such a case cannot be stable. Depending on the mesh design, on the thickness, on the elastic and on the density properties of the shallow layer, all terms of $\boldsymbol{\mathcal{A}}^\varepsilon$ potentially lead to instabilities when ε gets large enough. For order 2 terms, this stability issue is probably linked to the variational crime mention earlier. Nevertheless, this stability problem has not been an issue for any of the cases presented in this paper.

3 VALIDATION TESTS

All the validation tests presented in this paper are done in spherical geometry. This introduces a small modification of the boundary condition for the spheroidal part given in Appendix C. In order to validate the above theoretical development we first perform a test in the model 2 defined in the introduction. The source–receiver configuration is the same as the one used in Section 1. The reference solution is computed in model 2 using mesh 2. The order 0 asymptotic solution is obtained by computing the seismogams in model 1 using mesh 1. The results have already been shown in Section 1, Fig. 2, and are not accurate. On Fig. 7 is shown in dashed line the asymptotic solution for the order 1 (left-hand plots) and order 2 (right-hand plots) for the boundary condition and order 1 for the receiver and to be compared with the reference solution (solid line). The source used is not in the shallow layer (161 km deep), therefore, no correction is required for the source. This result has to be compared with the two approximate solutions used in the

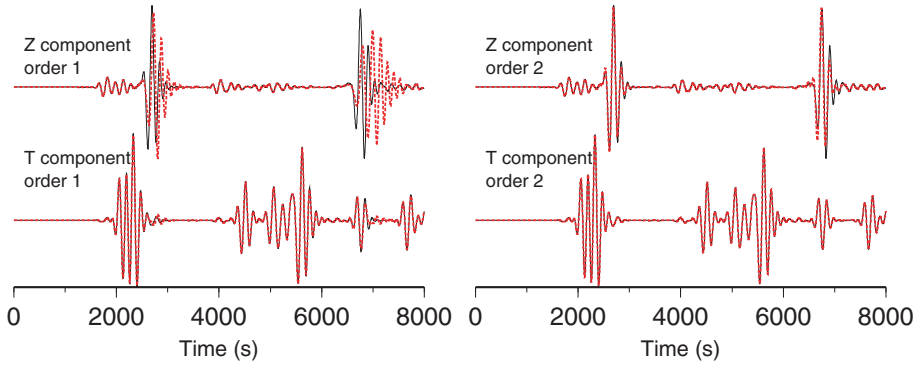

Figure 7. Comparison between reference seismograms (solid line) obtained in model 2 and solutions obtained in model 1 with the asymptotic boundary conditions at the order 1 (left-hand plots) and at the order 2 (right-hand plots) and with order 1 receiver correction. The geometrical configuration is the same as for Fig. 2. Residuals are shown Fig. 8.

introduction: removing the shallow layer (Fig. 2), which is actually the order 0 asymptotic solution, and using a mesh that doesn't honour the physical discontinuity with an element boundary (Fig. 3). It appears that the order 1 is accurate for the transverse component but not for the vertical one. On the transverse component, some small discrepancy with the reference solution can nevertheless be observed for times corresponding to the Rayleigh waves. This is due to the small transverse component of the spheroidal solution. The order 2 corrects a large part of the error observed for the order 1. This is still not perfect but far much better than any of the approximate solutions tried in the introduction. The only differences between the order 1 and 2 for the transverse component are due to the small transverse component of the spheroidal solution. Indeed, it appears that the order 1 for the toroidal solution is, in fact, the order 2 accuracy (the order 2 terms of the toroidal asymptotic expansion for the boundary condition are all zero). To have an idea of the convergence towards the reference solution as the thickness of the shallow layer decreases, a similar test with a layer thickness of 10 km has been performed. In Fig. 8 is shown the residuals between the reference solution and the solution obtained with the order 2 boundary conditions and the order 1 receiver solutions for the 20 km (solid line) and the 10 km (dashed line) thick shallow layer. It can first be observed that the residuals are larger for the vertical component than for the transverse component. For the vertical component, the residual amplitude is roughly divided by 8 between the 20 and 10 km layer thickness cases, which is coherent with an ε^3 asymptotic approximation. For the transverse component, some parts of the signal have indeed a residual amplitude divided by 8 but some others only by 4 or 2. This indicates that some parts of the residual signal is dominated by the boundary condition effects (order 2) and some other by the receiver correction (order 1) or even sphericity effects (order 0 for the transverse component). The last two effects are very small but still appear due to the good accuracy achieved for the transverse component. For applications requiring high accuracy convergence, it might be a good idea to go to the order 2 also for the receiver correction and all sphercity terms. The effect of the receiver correction is shown in Fig. 9. In this case, it can be seen that it affects slightly the amplitude for the fundamental surface wave

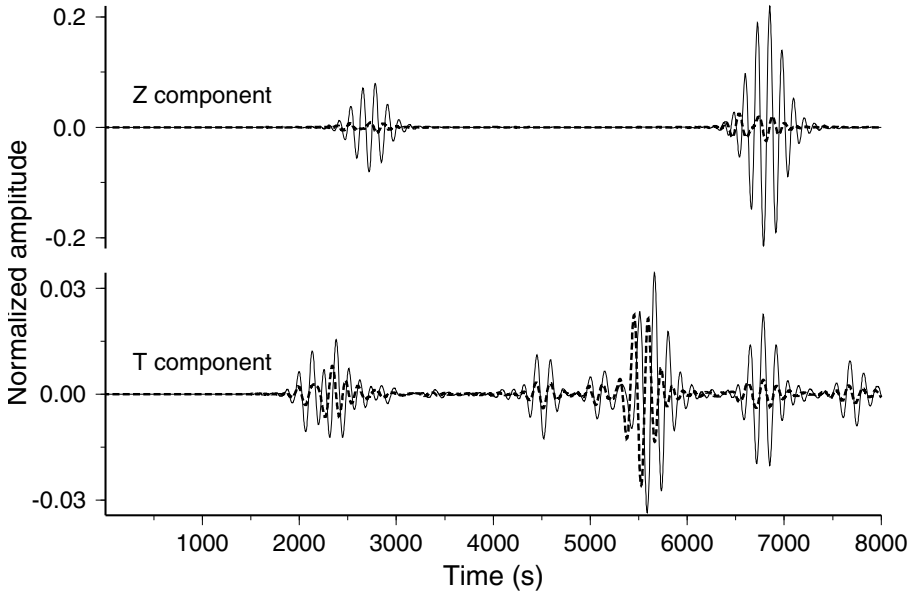

Figure 8. Residuals between the reference solution and the solution obtained with the order 2 boundary condition and the order 1 receiver solutions in model 2 with a 20 km (solid line) and a 10 km (dashed line) thick shallow layer. The amplitude of the traces is normalized with the maximum amplitude of the reference solution.

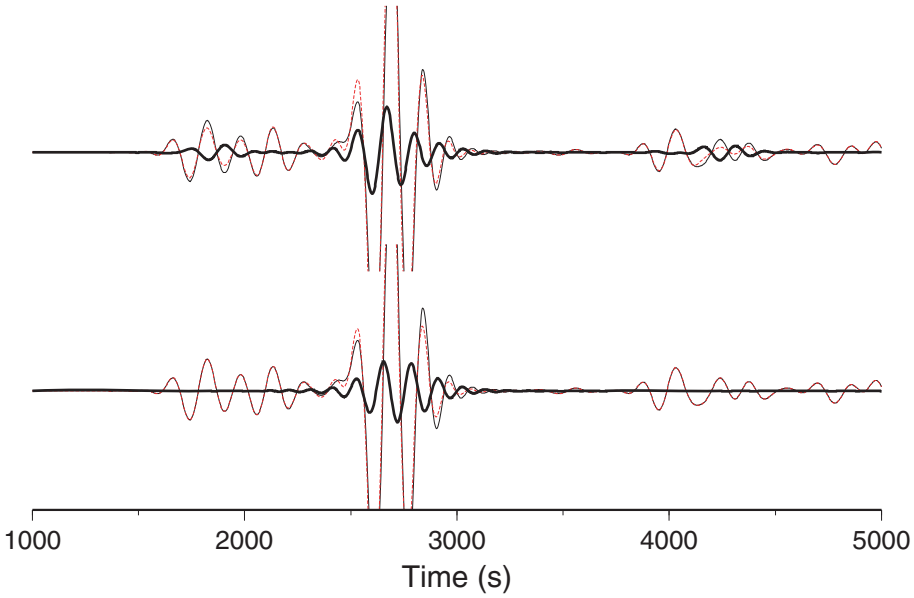

Figure 9. Effect of the order 1 local correction on the receiver. On the top traces is plotted the vertical component of the reference solution (thin solid line), the solution with order 2 asymptotic boundary condition and no correction at the receiver (dotted line) and the residual (bold solid line). On the bottom traces is plotted the same thing but this time the receiver correction is applied (dotted line).

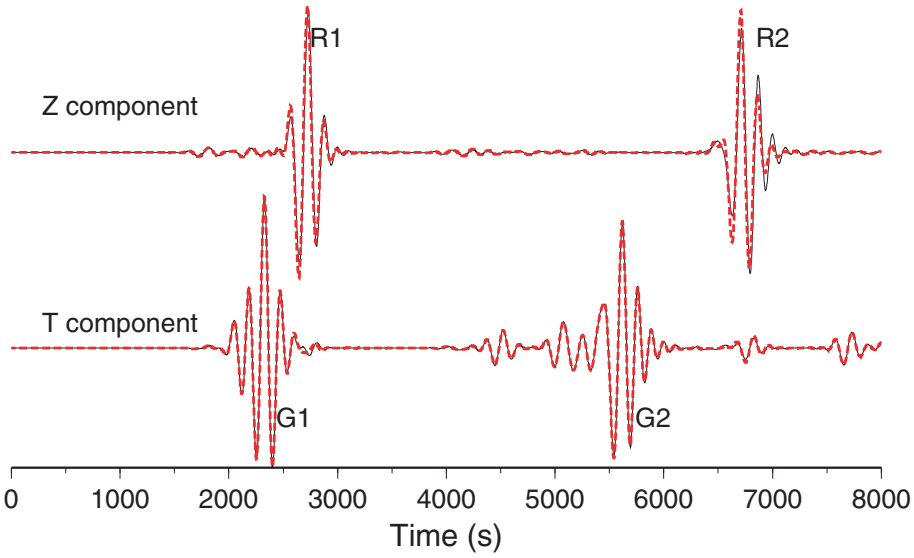

Figure 10. Same as Fig. 7 right-hand part, but this time, the source is 10 km depth (in the shallow layer) and an order 1 correction is applied for the source. This figure has to be compared with the approximate solutions Figs 4 and 5.

but mainly the amplitude of some higher modes. In Fig. 10 is shown the effect of the order 1 source correction if the source lies in the shallow layer. It can be seen that this correction accurately corrects the amplitude effects seen on Figs 4 and 5. Nevertheless, looking carefully, it appears that the accuracy is not as good (especially for the Rayleigh phase) as when the source is not in the shallow layer. This indicates that the order 2 correction for the source might be useful for higher accuracy.

Finally, we show a test in a more realistic Earth. We use PREMoc, a modified PREM model with a thin oceanic crust but no ocean (see Fig. 11). For this model, the Earth radius is 6366 km and the crustal thickness is 6.5 km. In Fig. 12 are shown traces obtained with different numerical simulations. The reference solution is computed in the PREMoc with a SEM mesh honouring all the model discontinuities and especially the Moho. Then, the solution corresponding to the order 0 of the asymptotic solution is shown. In that case the asymptotic solution is just a regular computation with free boundary condition in the order 0 model. The order 0 model corresponds to the elastic properties and density of the $\mathbf{S}^s$ operator for which the crustal layer has been replaced by the continuity of the mantle (see Fig. 11, right-hand graph). Note that here the order 0 model is not constant in the shallow layer but is a degree 1 polynomial: the prolongation of the PREMoc upper mantle. The traces obtained in such a model have surface wave phases heavily shifted with respect to the reference solution which shows how inaccurate this solution is (Fig. 12). Next is computed the solution in PREMoc, but with a SEM mesh that doesn't honour the Moho. Instead the mesh interface that corresponds to the Moho is moved down by 20 km to a

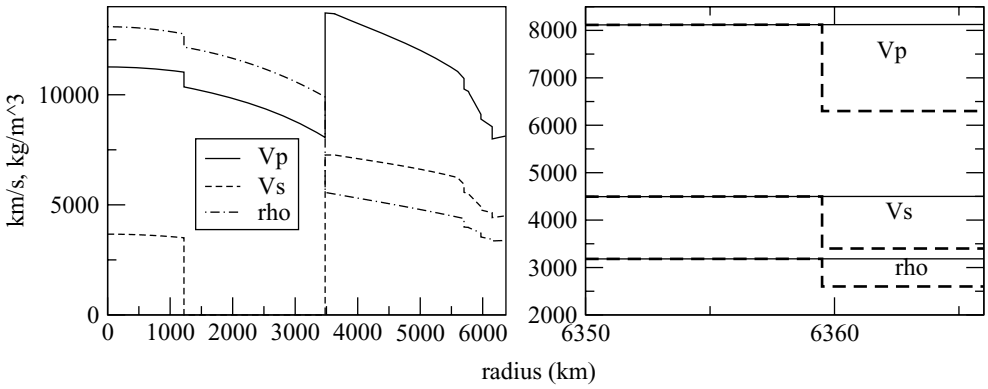

Figure 11. *P* and *S* wave velocities (*Vp* and *Vs*) and density (rho) as a function of the Earth radius of the PREMoc model, a modified PREM model used for the last numerical experiment of this paper. It is a modified PREM in the sense that the Earth radius in 6366 km (6371 km for the original PREM), the Moho depth is 6.5 km (24.4 km for the original PREM) and crustal properties correspond to an oceanic crust (obtained from CRUST2.0). On the left is plotted an Earth scale view of the model. On the right is plotted a zoom of rho, Vp and Vs in the last kilometres of PREMoc (dashed lines) and of the order 0 model (solid line) used for the asymptotic method. The last model correspond to the elastic properties and density of the $\mathbf{S}^s$ operator.

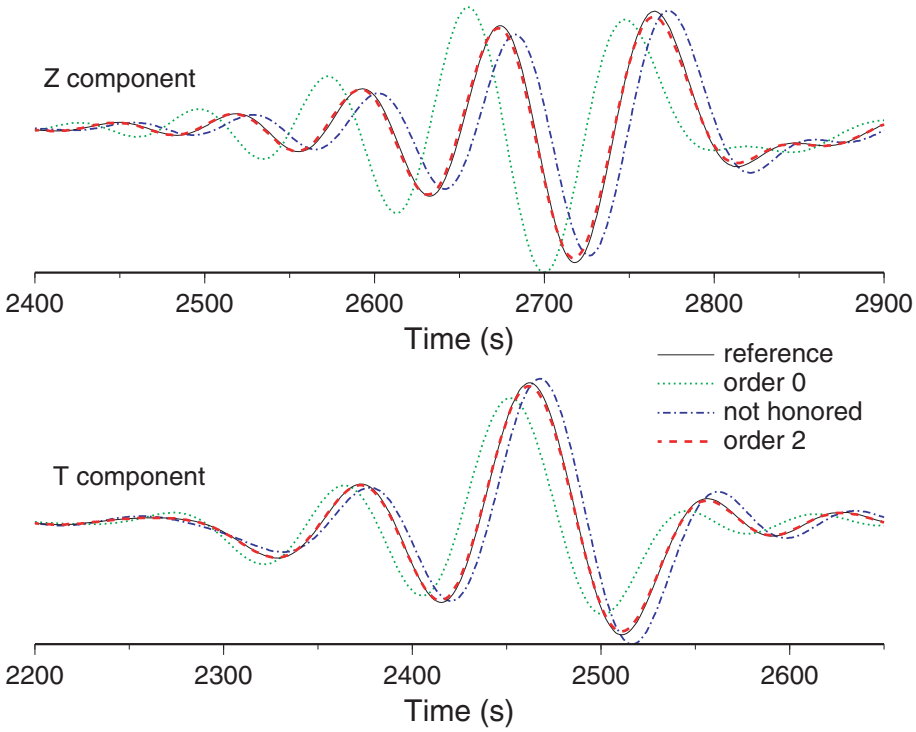

Figure 12. Vertical (top traces) and transverse (bottom traces) components for the experiment in PREMoc (Fig. 11). The reference solution (solid lines) is computed in PREMoc with a mesh honouring all the interfaces and especially the Moho. In dotted line is plotted the solution computed in the order 0 model, that is a model for which the crust has been removed and replaced by the continuity of the mantle (see Fig. 11, right-hand plot). In dash–dotted line is plotted the solution computed in PREMoc but with a mesh that is not honouring the Moho discontinuity (the mesh interface corresponding the Moho have been placed at 20 km depth, which corresponds to the Moho depth of the real PREM). In dashed line is plotted the solution computed with the order 2 asymptotic boundary condition and the order 1 receiver corrector. The corner frequency of the source is 1/65 Hz and is an irrelevant moment tensor. The time windows are focused on the minor arc surface waves. The source depth is 25 km and the epicentral distance is 77°.

depth that corresponds to the Moho depth of the real PREM. This represents the solution that is commonly used in global seismology. It can be seen that this solution is more accurate than the previous one, but the error is still very large. The phase shift is this time overestimated where as in the example given Fig. 3, the phase shift is underestimated. This shows how unpredictable is the error when major model discontinuities are not honoured by a mesh interface. Finally, the order 2 asymptotic solution is shown. The accuracy is really good despite a small amplitude error. For this example, just because of the time step, the computation of the asymptotic solution is here seven times faster than that of the reference solution.

4 DISCUSSION, CONCLUSION AND PERSPECTIVES

We have presented a second order asymptotic method to compute the effective behaviour of the wavefield in the presence of a thin

heterogeneous shallow layer below the free surface. Using an order 2 matching asymptotic expansion, we have shown that, in the case of a shallow layer thickness much smaller than the minimum wavelength of the wavefield, the shallow layer elastic and density properties can be removed and replaced by continuation of the elastic and density properties of the medium just below the shallow layer and by a particular DtN boundary condition. From the numerical method point of view, the main interest of such a method is that the shallow layer lower boundary doesn't exist anymore and, therefore, doesn't need to be matched by a mesh interface. This releases the meshing and explicit time marching time step problems. It has been shown, that if the thickness is small enough with respect to the minimum wavelength, the accuracy is excellent. The actual 'small enough' thickness required widely varies with the actual properties of the elastic medium in the shallow layer and the wanted accuracy. In the example given in this paper the ratio thickness with respect to the horizontal wavelength is as small as 1/30, but is can raise up to 5 for smaller velocity contrasts.

The SEM implementation of the DtN boundary condition can lead to an unstable Newmark time scheme if the thin layer is not thin enough compared to the minimum wavelength that can accurately be sampled by the mesh. This can be a serious problem in some situations. For example, if the thickness of the shallow layer is smoothly varying laterally and becoming locally too thick so the time scheme is unstable, the asymptotic solution cannot be used at all. This problem can be solved using a spatial filtering of the displacement wavefield at the surface before using it in the boundary condition DtN operator. The spacial filtering removes the unphysical high spatial frequencies of the wavefield and leads to a stable scheme. Another potential solution in the introduction of auxiliary variables following the work on non-reflecting absorbing boundaries (Givoli 2004). These solutions will be explored in the near future. Nevertheless, even if the scheme can be made stable in any case, it doesn't improve the fact that the accuracy that decreases rapidly when the thickness of the layer is no longer small enough compared the wavelength. This is the main limitation of this development: the frequency range of accuracy is determined by the geometry (mainly the thickness of the shallow layer) of the model. When the thin layer assumption is broken by increasing the corner frequency of the source or by increasing the thickness of the shallow layer, the accuracy deteriorates and this development needs to be dropped. Another obvious limitation is that this work only applies to small scales directly located below the free surface and doesn't help for deeper small scale heterogeneities. An option to go around these two problems is to move to volume homogenization (Capdeville & Marigo 2007). In Capdeville & Marigo (2007), it is shown that, for a given frequency band, an effective model and wave equation can be found. In the layered model case, the order 2 effective medium is a Backus filtering (Backus 1962) of the original model in the volume together with a DtN boundary condition for the free surface similar to the one obtained here. In that case, a different but valid solution is found for each frequency band and for any depth of the small scale heteogenities. The SEM implementation of Capdeville & Marigo (2007)'s work will be the purpose of a future publication.

Applications of this work as it stands should be found in forward modelling as it allows to take into account complex shallow structures. A good example of such an application is the accurate implementation of crustal models at the global scale. Such a technique is of course not limited to the global scale and can be applied for example at the scale of a basin to take accurately into account a shallow structure like a sediment layer. A following application is the crustal correction for imaging technique. Indeed, for classical seismic imaging techniques, the crust is not inverted for, but an *a priori* crustal model is used. By allowing to incorporate accurately the *a priori* crustal model in the forward modelling problem, this work can be used to solve this classical problem. This work can also be used for seismic imaging by allowing to invert for the crust. Indeed, this works gives an integrated parametrization of these complex shallow structures and of the local sources and receivers interaction with the small scale of the Earth through a limited numbers of parameters (X_L^1, X_N^1, etc.) that can be inverted for more easily than a thin vertical parametrization of the crust.

ACKNOWLEDGMENTS

This work has been funded by the French ANR MUSE project under the BLANC program. Computations were performed on IPGP's cluster, IDRIS and CINES computers. Many thanks to Jean-Pierre Vilotte, Jean-Paul Montagner and B. Romanowicz as well as Qinya Liu and an anonymous reviewer for their help to improve the manuscript. Many thanks to Dan Givoli and to Paco Sánchez-Sesma for pointing out my variational crime.

REFERENCES

Abdelmoula, R. & Marigo, J.-J., 2000. The effective behavior of a fiber bridged crack, *J. Mech. Phys. Solids,* **48**(11), 2419–2444.

Allaire, G. & Amar, M., 1999. Boundary layer tails in periodic homogenization, *ESAIM Control Optim. Calc. Var.,* **4,** 209–243 (electronic).

Amar, M., 2000. A note on boundary layer effects in periodic homogenization with Dirichlet boundary conditions, *Discrete Contin. Dyn. Syst.,* **6**(3), 537–556.

Backus, G., 1962. Long-wave elastic anisotropy produced by horizontal layering, *J. geophys. Res.,* **67**(11), 4427–4440.

Bassin, C., Laske, G. & Masters, G., 2000. The current limits of resolution for surface wave tomography in north America, *EOS, Trans. Am. geophys. Un.,* **81,** F897.

Boutin, C. & Roussillon, P., 2006. Wave propagation in presence of oscillators on the free surface, *Int. J. Engrg. Sci.,* **44,** 180–204.

Capdeville, Y. & Marigo, J.J., 2007. Second order homogenization of the elastic wave equation for non-periodic layered media, *Geophys. J. Int.,* **170,** 823–838.

Capdeville, Y., Chaljub, E., Vilotte, J.P. & Montagner, J.P., 2003. Coupling the spectral element method with a modal solution for elastic wave propgation in global earth models, *Geophys. J. Int.,* **152,** 34–66.

Chaljub, E., 2000. Modèlisation numérique de la propagation d'ondes sismiques à l'échelle du globe, *Thèse de doctorat, de l'Université Paris 7.*

Chaljub, E., Capdeville, Y. & Vilotte, J., 2003. Solving elastodynamics in a solid heterogeneous 3-Sphere: a spectral element approximation on geometrically non-conforming grids, *J. Comput. Phys.,* **183,** 457–491.

Choblet, G., 2005. Modelling thermal convection with large viscosity gradients in one block of the 'cubed sphere', *J. Comput. Phys.,* **205,** 269–291.

Dumontet, H., 1986. Study of a boundary layer problem in elastic composite materials, *RAIRO Modél. Math. Anal. Numér.,* **20**(2), 265–286.

Dziewonski, A.M. & Anderson, D.L., 1981. Preliminary reference Earth model, *Phys. Earth planet. Int.,* **25,** 297–356.

Faccioli, E., Maggio, F., Quarteroni, A. & Tagliani, A., 1996. Spectral-domain decomposition methods for the solution of acoustic and elastic wave equations, *Geophysics,* **61**(4), 1160–1174.

Givoli, D., 2004. High-order local non-reflecting boundary conditions: a review, *Wave Motion,* **39,** 319–326.

Givoli, D., Hagstrom, T. & Patlashenko, I., 2006. Finite element formulation with high-order absorbing boundary conditions for time-dependent waves, *Comput. Methods Appl. Mech. Engrg.,* **195,** 3666–3690.

Komatitsch, D. & Tromp, J., 2002. Spectral-element simulations of global seismic wave propagation, part II: 3-D models, oceans, rotation, and gravity, *Geophys. J. Int.,* **150,** 303–318.

Komatitsch, D. & Vilotte, J.P., 1998. The spectral element method: an effective tool to simulate the seismic response of 2d and 3d geological structures, *Bull. seism. Soc. Am.,* **88,** 368–392.

Leonach, B. & Grover, B., 2000. A homogenisation approach to elastic waves in directional media, *Wave Motion,* **31,** 209–222.

Marone, F. & Romanowicz, B., 2007. Non-linear crustal corrections in high-resolution regional waveform seismic tomography, *Geophys. J. Int.,* **170,** 460–467.

Montagner, J.P. & Jobert, N., 1988. Vectorial tomography–II. Application to the Indian Ocean, *Geophys. J.,* **94,** 309–344.

Nataf, H.C. & Ricard, Y., 1996. 3SMAC: an a priori tomographic model of the upper mantle based on geophysical modeling, *Phys. Earth planet. Int.,* **95,** 101–122.

Nguetseng, N. & Sanchez-Palencia, E., 1985. Stress concentration for defects distributed near a surface, in *Local Effects in the Analysis of Structures (Cachan, 1984)*, Vol. 12 of *Stud. Appl. Mech.*, pp. 55–74, Elsevier, Amsterdam.

Priolo, E., Carcione, J.M. & Seriani, G., 1994. Numerical simulation of interface waves by high-order spectral modeling techniques, *J. acoust. Soc. Am.,* **95**(2), 681–693.

Ronchi, C., Ianoco, R. & Paolucci, P.S., 1996. The 'Cubed Sphere': a new method for the solution of partial differential equations in spherical geometry, *J. Comput. Phys.,* **124,** 93–114.

Sadourny, R., 1972. Conservative finite-difference approximations of the primitive equation on quasi-uniform spherical grids, *Mon. Wea. Rev.,* **100,** 136–144.

Sanchez-Palencia, E., 1987. Boundary layers and edge effects in composites, in *Homogenization Techniques for Composite Media (Udine, 1985)*, Vol. 272 of *Lecture Notes in Physics*, pp. 121–192. Springer, Berlin.

Strang, G. & Fix, G.J., 1973. *An Analysis of the Finite Element Method*, Prentice-Hall, Englewood Cliffs.

Takeuchi, H. & Saito, M., 1972. Seismic surface waves, *Methods Comput. Phys.,* **11,** 217–295.

APPENDIX A: SECOND ORDER EXPRESSION OF THE BOUNDARY CONDITION

For the toroidal case, one can check that the ε^2 terms for the asymptotic boundary condition is 0. Therefore, expression (62) is also valid for the order 2.

For the spheroidal case the matching condition (50) gives

$$\left[(\mathbf{I} - \varepsilon\, {}_s\hat{\mathbf{X}}^2_k)_s \hat{\boldsymbol{\mathcal{Y}}}^1_k\right]_{2,4}(a) = 0, \tag{A1}$$

which can be written as

$$T_{Uk}(a,\omega) = -\varepsilon\omega^2 X^1_\rho(0) U_k(a,\omega) + \varepsilon^2\left[k\omega^2 X^2_a(0) + k^3 X^2_{a1}(0)\right] V_k(a,\omega) \tag{A2}$$

$$T_{Vk}(a,\omega) = \varepsilon\left[k^2 X^1_{a1} - \omega^2 X^1_\rho(0)\right] V_k(a,\omega) + \varepsilon^2\left[k\omega^2 X^2_b(0) + k^3 X^2_{a1}\right] U_k(a,\omega), \tag{A3}$$

where all terms higher than ε^2 have been truncated, and

$$X^1_{a0}(y) = -\int_y^{y_a} \left[a_0(y') - a^s_0(a)\right] \mathrm{d}y' \tag{A4}$$

$$X^1_{a1}(y) = -\int_y^{y_a} \left[a_1(y') - a^s_1(a)\right] \mathrm{d}y' \tag{A5}$$

$$X^2_{a1}(y) = -\int_y^{y_a} \left[X^1_{a1}(y') - X^1_{a1}(0)\right] \mathrm{d}y' \tag{A6}$$

$$X^2_a(y) = \int_y^{y_a} \left\{ \rho(y')\left[X^1_{a0}(y') - X^1_{a0}(0)\right] + \left[1 - a^s_0(a)\right]\left[X^1_\rho(y') - X^1_\rho(0)\right] \right\} \mathrm{d}y' \tag{A7}$$

$$X^2_b(y) = \int_y^{y_a} \left\{ \rho^s(a)\left[X^1_{a0}(y') - X^1_{a0}(0)\right] + \left[1 - a_0(y')\right]\left[X^1_\rho(y') - X^1_\rho(0)\right] \right\} \mathrm{d}y' + X^1_{a0}(0) X^1_\rho(0), \tag{A8}$$

where for any function f^ε, $f(y) = f^\varepsilon(\varepsilon y + b)$. Furthermore, using that fact that

$$\frac{\mathrm{d}}{\mathrm{d}y}\left[X^1_\rho(y) - X^1_\rho(0)\right] = \rho(y) - \rho^s(a), \tag{A9}$$

and

$$\frac{\mathrm{d}}{\mathrm{d}y}\left[X^1_{a0}(y) - X^1_{a0}(0)\right] = a_0(y) - a^s_0(a), \tag{A10}$$

it can be shown with some algebra that $X^a_2(0) = X^b_2(0)$.

Using expressions (3) and (5), properties (18)–(20), the fact that

$$\boldsymbol{\nabla}_1 \cdot \mathbf{B}_{km} = -k\mathbf{P}_{km} \cdot \hat{\mathbf{z}}, \tag{A11}$$

$$\boldsymbol{\nabla}_1 (\mathbf{P}_{km} \cdot \hat{\mathbf{z}}) = k\mathbf{B}_{km}, \tag{A12}$$

and the identity (23) we find from (A2) and (A3)

$$\mathrm{t}_z^{PSV} = \varepsilon X_\rho^1 \ddot{\mathrm{u}}_z + \varepsilon^2 X_a^2 \, \boldsymbol{\nabla}_1 \cdot \ddot{\mathbf{u}}_1 + \varepsilon^2 X_{a1}^2 \, \nabla_1^2 (\boldsymbol{\nabla}_1 \cdot \mathbf{u}_1) \tag{A13}$$

$$\mathbf{t}_1^{PSV} = -\varepsilon X_{a1}^1 \, \boldsymbol{\nabla}_1 (\boldsymbol{\nabla}_1 \cdot \mathbf{u}_1) + \varepsilon X_\rho^1 \ddot{\mathbf{u}}_1^{PSV} - \varepsilon^2 X_b^2 \, \boldsymbol{\nabla}_1 \ddot{\mathrm{u}}_z - \varepsilon^2 X_{a1}^2 \, \nabla_1^2 (\boldsymbol{\nabla}_1 \mathrm{u}_z), \tag{A14}$$

where the X coefficients are taken in $y = 0$ and the traction and displacement in $(\mathbf{x}, t)$, $\mathbf{x}$ belonging to the free surface. Using $\mathbf{t} = \mathbf{t}_1^{PSV} + \mathrm{t}_z^{PSV} \hat{\mathbf{z}} + \mathbf{t}^{SH}$ and $\mathbf{u} = \mathbf{u}_1^{PSV} + \mathrm{u}_z^{PSV} \hat{\mathbf{z}} + \mathbf{u}^{SH}$, we find, for all $\mathbf{x}$ belonging to the free surface and all time t

$$\mathbf{t} = \boldsymbol{\mathcal{A}}^\varepsilon (\mathbf{u}, \ddot{\mathbf{u}}), \tag{A15}$$

with

$$\begin{aligned} \boldsymbol{\mathcal{A}}^\varepsilon (\mathbf{u}, \ddot{\mathbf{u}}) = {} & \varepsilon \left\{ X_\rho^1 \ddot{\mathbf{u}} - X_{a1}^1 \, \boldsymbol{\nabla}_1 (\boldsymbol{\nabla}_1 \cdot \mathbf{u}_1) + X_N^1 \, \boldsymbol{\nabla}_1 \times \boldsymbol{\nabla}_1 \times \mathbf{u}_1 \right\} \\ & + \varepsilon^2 \left\{ X_{a1}^2 \nabla_1^2 \left[(\boldsymbol{\nabla}_1 \cdot \mathbf{u}_1) \hat{\mathbf{z}} - \boldsymbol{\nabla}_1 \mathrm{u}_z \right] + X_b^2 \, \left[(\boldsymbol{\nabla}_1 \cdot \ddot{\mathbf{u}}_1) \hat{\mathbf{z}} - \boldsymbol{\nabla}_1 \ddot{\mathrm{u}}_z \right] \right\}, \end{aligned} \tag{A16}$$

where the X coefficients are taken in $y = 0$. As written here, (A16) leads to a non-symmetric term in (81). Nevertheless, because $X_a^2 = X_b^2$, it can be symmetrize. This can be seen on the spectral expressions (A2) and (A3) or directly on (A16) following the same procedure as Chaljub (2000) for the gravity terms in the wave equation.

APPENDIX B: SPHEROIDAL CONTRIBUTION TO THE SOURCE CORRECTION

We develop here the order 1 spheroidal contribution to the correction to be applied to source if it is located in the shallow layer. Starting from

$$\mathbf{M} : \boldsymbol{\nabla} \mathbf{u} = \mathbf{M}_{11} : \boldsymbol{\epsilon}_{11} + \mathbf{M}_{1z} \cdot (\boldsymbol{\nabla}_1 \mathrm{u}_z + \partial_z \mathbf{u}_1) + M_{zz} \mathrm{u}_z, \tag{B1}$$

and considering the following spheroidal displacement for any k and m,

$$\mathbf{u}^c = U_k^c \mathbf{P}_{km} + V_k^c \mathbf{B}_{km}, \tag{B2}$$

we have, for any $\mathbf{M}$,

$$M_{zz} \mathrm{u}_z^c = \partial_z U_k^c M_{zz} \mathbf{P}_{km} \cdot \hat{\mathbf{z}}, \tag{B3}$$

$$\mathbf{M}_{1z} \cdot \left(\boldsymbol{\nabla}_1 \mathrm{u}_z^c + \partial_z \mathbf{u}_1^c \right) = \frac{1}{L_e^\varepsilon} T_{Vk}^c \mathbf{M}_{1z} \cdot \mathbf{B}_{km}, \tag{B4}$$

$$\mathbf{M}_{11} : \boldsymbol{\epsilon}_{11}^c = V_k^c \mathbf{M}_{11} : \boldsymbol{\nabla}_1 \mathbf{B}_{km}. \tag{B5}$$

Using (54) and (55) for the spheroidal case, to the first order we find

$$V_k^c = V_k - \varepsilon L_e^s X_{eL}^1 \left(\partial_z V_k + k U_k \right), \tag{B6}$$

$$T_{Vk}^c = T_{Vk} - \varepsilon k X_{ea0}^1 C_e^s \partial_z U_k - \varepsilon \left[k^2 \left(X_{ea1}^1 - F_e^s X_{ea0}^1 \right) - \omega^2 X_{e\rho}^1 \right] V_k, \tag{B7}$$

$$\partial_z U_k^c = \frac{C_e^s}{C_e^\varepsilon} \partial_z U_k + k \frac{F_e^\varepsilon - F_e^s}{C_e^\varepsilon} V_k + \varepsilon \omega^2 \frac{X_{e\rho}^1}{C_e^\varepsilon} U_k - \varepsilon k a_{e0}^\varepsilon L_e^s X_{eL}^1 (\partial_z V_k + k U_k), \tag{B8}$$

where $C_e^\varepsilon = C^\varepsilon(z_e)$, $C_e^s = C^s(z_e)$, $F_e^\varepsilon = F^\varepsilon(z_e)$, $F_e^s = F^s(z_e)$,

$$X_{ea0}^1 = X_{a0}^1(0) - X_{a0}^1 \left(\frac{z_e - b}{\varepsilon} \right), \tag{B9}$$

$$X_{ea1}^1 = X_{a1}^1(0) - X_{a1}^1 \left(\frac{z_e - b}{\varepsilon} \right). \tag{B10}$$

Using (20), (23), (A11), $\mathbf{I} : \boldsymbol{\nabla}_1 \mathbf{B}_{km} = -k \mathbf{P}_{km} \cdot \hat{\mathbf{z}}$ and combining with the toroidal solution, we finally have

$$\begin{aligned} \mathbf{M}^c : \boldsymbol{\epsilon}^c = {} & \mathbf{M}^0 : \boldsymbol{\epsilon} \\ & - \varepsilon X_{eL}^1 L_e^s \mathbf{M}_{11}^c : (\partial_z \boldsymbol{\epsilon}_{11} + \boldsymbol{\nabla}_1 \boldsymbol{\nabla}_1 \mathrm{u}_z) + \varepsilon a_{e0} X_{eL}^1 L_e^s \, M_{zz}^c \left(\boldsymbol{\nabla}_1 \cdot \partial_z \mathbf{u}_1 + \nabla_1^2 \mathrm{u}_z \right) \\ & - \varepsilon X_{ea0}^1 \frac{C_e^s}{L_e^s} \mathbf{M}_{1z}^0 \cdot \boldsymbol{\nabla}_1 \partial_z \mathrm{u}_z + \varepsilon \omega^2 \frac{X_{e\rho}^1}{L_e^s} \mathbf{M}_{1z}^0 \cdot \mathbf{u}_1 + \varepsilon \omega^2 \frac{X_{e\rho}^1}{C_e^s} M_{zz}^0 \mathrm{u}_z \\ & + \varepsilon \frac{X_{ea1}^1 - F_e^s X_{ea0}^1}{L_e^s} \mathbf{M}_{1z}^0 \cdot \boldsymbol{\nabla}_1 (\boldsymbol{\nabla}_1 \cdot \mathbf{u}_1) - \varepsilon \frac{X_{eN}^1}{L_e^s} \mathbf{M}_{1z}^0 \cdot (\boldsymbol{\nabla}_1 \times \boldsymbol{\nabla}_1 \times \mathbf{u}_1), \end{aligned} \tag{B11}$$

where

$$M_{zz}^0 = M_{zz}^c \frac{C_e^s}{C_e^\varepsilon} \tag{B12}$$

$$M^0_{rr} = M^c_{rr} + M^c_{zz}\frac{F^s_e - F^\varepsilon_e}{C^\varepsilon_e} \tag{B13}$$

$$M^0_{\phi\phi} = M^c_{\phi\phi} + M^c_{zz}\frac{F^s_e - F^\varepsilon_e}{C^\varepsilon_e} \tag{B14}$$

$$M^0_{zr} = M^c_{zr}\frac{L^s_e}{L^\varepsilon_e} \tag{B15}$$

$$M^0_{z\phi} = M^c_{z\phi}\frac{L^s_e}{L^\varepsilon_e} \tag{B16}$$

$$M^0_{r\phi} = M^c_{r\phi}. \tag{B17}$$

These last expressions give the order 0 effect of the shallow layer on the source. This result is the same than the one obtain by Capdeville & Marigo (2007). As it has been done for the toroidal case, (B11) can be rewritten as

$$\mathbf{f}(\mathbf{x}, t) = \mathcal{F}[f(t)\delta(\mathbf{x} - \mathbf{x}_e)], \tag{B18}$$

where the operator $\mathcal{F}$ can be derived from (B11).

Spectral element implementation of a source in the shallow layer is similar as the implementation of the boundary condition. It nevertheless requires to compute the surface gradient of a vector, which, in spherical geometry using the 'cubed sphere' coordinate system is not completely trivial. Useful formula for this point can be found in Choblet (2005).

APPENDIX C: EFFECT OF SPHERICITY

For the sake of simplicity, this paper has been written for the flat geometry. Nevertheless, for large applications, including the examples given in this paper, the sphericity is important. Working in spherical geometry leads to the same generic eq. (9) with similar matrices (10) and (11) (see Takeuchi & Saito 1972, for details):

$${}_s\mathbf{S}_l(r, \omega) = \begin{bmatrix} d/r & 1/C & e_l/r & 0 \\ -\rho\omega^2 + a & -d/r & (-a\gamma_l + 2\rho g r)/2 & \gamma_l/r \\ -\gamma_l/r & 0 & 2/r & 1/L \\ (a\gamma_l + 2\rho g r)/2 & -e_l/r & -\rho\omega^2 + b_l & -2/r \end{bmatrix} \tag{C1}$$

with

$$a = \frac{4}{r^2}\left(A - \frac{F^2}{C} - N - \rho g r\right), \quad b_l = \frac{\gamma_l^2}{r^2}\left(A - \frac{F^2}{C}\right) - \frac{2N}{r^2},$$
$$d = 1 - \frac{2F}{C}, \quad e_l = \gamma_l\frac{F}{C}.$$

where g is the norm of the gravity field at the radius r and $\gamma_l = \sqrt{l(l+1)}$. In the toroidal case, we have:

$${}_t\mathbf{S}_l(r, \omega) = \begin{pmatrix} 2/r & 1/L \\ -\rho\omega^2 + \Omega_l N/r^2 & -2/r \end{pmatrix}, \tag{C2}$$

with $\Omega_l = (l-1)(l+2)$ and l the angular degree.

For our frequency range of interest, l is large enough such that $kr \simeq l + \frac{1}{2} \simeq \sqrt{\Omega_l} \simeq \gamma_l$, where k is the horizontal wave number used all along this paper. Assuming the asymptotic expansion is performed close to the free surface, we have $k \gg \frac{1}{r}$. Simplifying (C1) and (C2), we find the same expression than (10) and (11) but for two terms:

$$[{}_s\mathbf{S}_k]_{23} = -[{}_s\mathbf{S}_k]_{32} \simeq -\frac{2k}{r_{\partial\mathbf{\Omega}}}(a_1 - N), \tag{C3}$$

where $r_{\partial\Omega}$ is the earth radius. This requires to add $\varepsilon\frac{2}{r_{\partial}\mathbf{\Omega}}[X^1_{a1}(0) - X^1_N(0)]\,(\boldsymbol{\nabla}_1 \cdot \mathbf{u}_1\,\hat{\mathbf{z}} - \boldsymbol{\nabla}_1 \mathrm{u}_z)$ to expression (A16).